

Stony Brook University



OFFICIAL COPY

The official electronic file of this thesis or dissertation is maintained by the University Libraries on behalf of The Graduate School at Stony Brook University.

© All Rights Reserved by Author.

A Sharp Boundary Model for Electrocardiac Simulations

A Dissertation Presented

by

Shuai Xue

to

The Graduate School

in Partial Fulfillment of the

Requirements

for the Degree of

Doctor of Philosophy

in

Applied Mathematics and Statistics

Stony Brook University

May 2015

Stony Brook University
The Graduate School

Shuai Xue

We, the dissertation committee for the above candidate for the
Doctor of Philosophy degree, hereby recommend
acceptance of this dissertation.

James Glimm, Dissertation Advisor
Professor, Dept. of Applied Mathematics and Statistics

Xiangmin Jiao, Chairperson of Defense
Associate Professor, Dept. of Applied Mathematics and Statistics

Roman Samulyak, Committee Member
Professor, Dept. of Applied Mathematics and Statistics

Scott Smolka, Outside Member
Professor, Dept. of Computer Science

This dissertation is accepted by the Graduate School

Charles Taber
Dean of the Graduate School

Abstract of the Dissertation

A Sharp Boundary Model for Electrocardiac Simulations

by

Shuai Xue

Doctor of Philosophy

in

Applied Mathematics and Statistics

Stony Brook University

2015

We present a sharp boundary electrocardiac simulation model based on the finite volume embedded boundary method for the solution of voltage dynamics in irregular domains with anisotropy and a high degree of anatomical detail. This method is second order accurate uniformly up to boundaries and is able to resolve small features without the use of fine meshes. This capability is necessary to enable the repeated simulations required for future verification and validation (V&V) and uncertainty quantification (UQ) studies of defibrillation, where fine-scale heterogeneities, such as those formed by small blood vessels play an important role and require resolution.

Contents

List of Figures	vii
List of Tables	viii
Acknowledgments	ix
1 Introduction	1
1.1 Overview and Motivation	1
1.2 Related Work	6
1.3 Dissertation Organization	9
2 Governing Equations	11
2.1 Bidomain Model	12
2.1.1 Model Equations	13
2.1.2 Boundary Conditions	16
2.2 Monodomain Model	18

3	Numerical Methods	20
3.1	Overview of Numerical Methods	20
3.1.1	Ghost Cell Method	20
3.1.2	Phase Field Method	22
3.1.3	Immersed Boundary Method	23
3.1.4	Finite Element Method	24
3.1.5	Immersed Interface Method	25
3.1.6	Embedded Boundary Method	27
3.2	Embeded Boundary Method	28
3.3	The Gradient Approximation at A Face Centroid	33
3.3.1	Normal Derivative Approximation	34
3.3.2	Parallel Derivative Approximation	36
3.4	Boundary Conditions	39
3.5	Calculation of Geometric Quantities Using Marching Tetrahedra Method	42
4	Verification	46
4.1	Poisson’s Equation in 3D Spherical Domain	46
4.2	Comparison of EBM and PF	48

5 Applications	52
5.1 Defibrillation Simulation	55
5.2 Mesh Resolution	57
6 Conclusions	60

List of Figures

3.1	Stencil for the approximation of the normal derivative at the face centroid.	35
3.2	Stencil for the approximations of the parallel derivatives at the face centroid.	37
3.3	Stencil for the approximation of the derivatives at the boundary centroid.	40
3.4	Divide each cube into six tetrahedra.	43
3.5	Different configurations of tetrahedra cut by the embedded interface. .	45
5.1	Transmembrane potential (mV) in a slab before applying the defibrillation shock.	53
5.2	Cross section view of the transmembrane potential before applying the defibrillation shock.	54
5.3	Transmembrane potential (mV) in a slab after applying the defibrillation shock.	56
5.4	Variation of the voltage drop across the blood vessel under mesh refinement.	58

List of Tables

4.1	Orders of convergence for three types of errors	49
4.2	CV error and convergence order comparison	51
4.3	$V(L_1\text{-norm})$ error and convergence order comparison	51

Acknowledgments

I gratefully acknowledge my advisor, Professor James Glimm, for the interesting topic suggested and for his guidance and continuous support. I benefited a lot from his broad knowledge and innovative thinking.

It is a great honor to have Professor Xiangmin Jiao, Professor Roman Samulyak and Professor Scott Smolka to be my dissertation committee members. I really appreciate all the valuable suggestions they made to improve and perfect this dissertation.

Special thanks goes to Dr. Hyunkyung Lim for so many discussion we have together, which greatly influence the development and refinement of the high order sharp boundary method proposed in this thesis. I also appreciate much about her help in assisting me debugging the code and setting up a variate of simulations.

I would also like to thank Dr. Shuqiang Wang. I benefited a lot from discussions with him on the topics including C++ design patterns, usage of the PETSc library and the embedded boundary method.

Sincere thanks to my family, especially my wife Yan Zhan. It is your endless support and love that make me strong enough to face all the challenges during my pursue of the Ph.D. degree. I should never been able to overcome the endless difficulties in both studying and living without your encouragement.

Chapter 1

Introduction

1.1 Overview and Motivation

Heart failure is a leading cause of death in the industrial world [1, 14]. Great efforts have been devoted to understanding the underlying physiological mechanisms for the normal and abnormal behaviour of the heart. As the "engine" of the circulatory system, the heart keeps pumping blood to provide oxygen and nutrients to the body, and also removes metabolic wastes from the organs. Since normal contractions of the heart depends largely on the electrical signals sent from the brain, the study of the electrical activities within the cardiac tissue plays a crucial role in understanding the physiological fundamentals of heart functions and the prevention and treatment of cardiac diseases [74].

Extensive experimental studies have been performed to investigate the electrical activities within the cardiac tissue which coordinate the mechanical contraction of the heart [27, 28, 43]. In the beginning of each mechanical contraction, the contral

signal sent from the brain triggers the opening of the sodium channels on myocyte membranes in the sino-atrial node, which initiates a rapid action potential upstroke. The local voltage gradient resulted by the upstroke in turn leads to the opening of the sodium channels in the neighbouring cells, which results in the propagation of the action potential wave across the cardiac tissue [57].

Although in-vivo and in-vitro experiments still remain the most trustworthy methods for testing the correctness of electrocardiac theories and propositions, numerical simulations are playing more and more important roles in studying the propagation of action potential waves in the cardiac tissue. Compared with experiments the numerical models have several advantages, among which strong explanatory abilities and economical benefits are prominent. For example, in the study of re-entry wave genesis and 3D vortex propagation [32], most experiments only document the action potential evolution on the heart surface, in contrast, with numerical simulation tools, scientists can easily visualize the deformation and translation of the vortices within the cardiac tissue, which in turn inspires the generation of new hypothesis. The economical benefits are easily seen by considering experiments in which cardiac tissues of human or other higher animals are involved.

Two different categories of mathematical models for the action potential propagation in cardiac tissue have been adopted by researchers in the field of electrocardiology, which reflects the existence of two different perspectives on the electrophysiological properties of the heart tissue. In the first approach, the cardiac tissue is treated as a discrete network of cells, which has a finite number of states. The future state of a given cell is determined by its current state and the states of its neighbours. The simple cellular automaton (CA) model [76] and coupled map lattices (CML) model [53] fall into this category. The main advantages of the discrete models are their simplicity

intuitiveness and simplicity, which resulted in their popularity in the early days when the computational resources were limited. However, the discreteness of cell states prevents them from being used to the study of rate-dependent effects and other important phenomena [9].

The other category consists of models of the continuous type. The underlying assumption of these models is that at the macroscopic scale the cardiac tissue can be viewed as a functional syncytium of electrically coupled cells [77], the validation of which has been shown by experiments [27, 29]. These models successfully remove the restriction of discrete models that the cell states must be discrete, which lends them to the investigation of a wider range of problems. The most popular continuous models are the bidomain and monodomain models. As the most complete model for describing electrocardiac phenomena, the bidomain model has been widely used in simulations such as action potential propagation in complex geometries [47], excitation and repolarization patterns [38], and currents injection into cardiac tissue [96], etc. However, since the bidomain model involves an implicit equation of the extracellular potential, the solution of which is time consuming, in early dates its application to 3D full heart simulations was prohibitive. To overcome this shortcoming, the monodomain simplification was proposed. By assuming the equality of the anisotropies in the intracellular and extracellular spaces, it achieved great simplification over the more complete model. It has been shown that in the absence of injection of currents in the extracellular space, the mono-domain model renders realistic solutions for a wide range of problems [46, 7, 75]. However, for some interesting applications, such as low energy defibrillations [70], this limitation is too restrictive for the monodomain model to be useful. In latter sections, we will review the monodomain and bidomain models in more detail.

Both the bidomain and monodomain models are of the reaction-diffusion type. The diffusion part describes the propagation of the action potential, and the reaction part corresponds to ionic currents through the cell membrane. A number of models of the ionic currents have been proposed at differing levels of complexity and completeness. The human ventricular myocyte model of Iyer et al. [49] includes as many as 67 variables. In contrast, the FitzHugh-Nagumo model [36] for general excitable media only involves two variables. Although complex models can better reproduce existing experimental results through careful selection of parameters, too many parameters often affect the model robustness and introduce inconsistencies between models of the same animal species and specific regions of the heart [13]. Moreover, the overhead of using these complex models in 3D simulations with the geometry of a real heart and reasonable mesh refinement is quite formidable.

To overcome the complexities of detailed cardiac cell models, several reduced models have been proposed [3, 25, 32]. Among the widely used reduced models, the Fenton-Karma (FK) three variable model is a typical, maintaining most of the quantitative properties of the more complicated models, while reducing the computational complexities significantly [30]. These properties have made the FK model popular in a wide range of studies, including vortex dynamics in the myocardium [32], mechanisms for discordant alternans [109], temperature effects [33, 35] and the promising field of low energy defibrillation [12, 34]. In this thesis, we adopt the FK model to describe the evolution of the transmembrane ionic currents, the details of which are given in the following sections.

The main result of this thesis is the introduction of a high order sharp boundary treatment of the voltage equation into cardiac models. From the perspective of mathematical physics, the reaction-diffusion equations in bidomain and monodomain models

are elliptic and parabolic equations. Several numerical methods have been developed for the solution of elliptic and parabolic equations in domains with complex geometries, among which the ghost cell method [103], phase field method [31], immersed boundary method [73], finite element method [91], immersed interface method [64], and embedded boundary method [50] have been more widely adopted. In this thesis we extended the embedded boundary method to solve elliptic and parabolic equations with anisotropic diffusion tensors. The resulting algorithm allows arbitrary order of accuracy in the L_∞ norm, and as implemented here with algorithm details included is second order accurate. Local mesh refinement techniques, such as, h-refinement [66] and p-refinement [100] can be adopted to improve the numerical resolution on coarse grids. Both the arbitrary order of accuracy and the second order details are new, for the case of tensor diffusion, as considered here. The code is based on the finite volume discretization of the voltage equation, based on the embedded boundary method (EBM). We solve the bidomain equations, representing the cardiac tissue as a syncytium of overlapping intracellular and extracellular domains [16], as is needed in defibrillation modelling. For this same purpose we emphasize the resolution of small myocardial discontinuities, such as blood vessels and infarct scars, which can become the substrate for producing virtual electrodes when defibrillation voltage is applied [110, 70].

The major motivation of this work is a planned verification and validation (V&V) and uncertainty quantification (UQ) study of defibrillating voltages applied at electrodes on the exterior of the heart as outlined by Pathmanathan et al. in [81]. The purpose of the voltage is to reset the electrical state of the heart, so that normal cycles of a heart beat will follow. Such V&V/UQ studies require repeated simulations, and their success depends in part on the number feasible within a given resource limit. Thus the ability to obtain useful solutions on a coarse mesh is the primary figure of

merit considered here, which is achieved by applying the high order numerical method introduced in this paper.

The implementation of the algorithms in this thesis uses an existing C++ EBM library developed by Dr. Shuqiang Wang as a starting point. Wang solved elliptic and parabolic equations in 2D and 3D geometries with complex geometries [108]. It should be noted that Wang’s EBM library is based on an earlier EBM library developed by Roman Samulyak and Jian Du, which is documented in [93].

1.2 Related Work

Our sharp boundary method is designed to perform highly accurate electrocardiac simulations on domains with complex geometries. Great effort has been devoted to this field to investigate the underlying mechanics of a wide range of electrocardiac phenomena with more and more anatomical details included. In the following paragraphs, we will review related electrocardiac simulation studies with a focus on both the numerical methods adopted and the physiological problems investigated.

As one of the most widely adopted numerical simulation tools in electrocardiology, the immersed boundary method (IBM) was developed by Peskin [85] in 1970s for the study of flow patterns around heart valves. For its capability to model general fluid-structure interactions, IBM has been applied in a variety of scientific studies, such as cochlea modelling [6], biofilm processing [23], valveless pumping [52], and fluid dynamics [69]. In IBM the interaction of elastic material and an incompressible viscous fluid is handled mathematically by the introduction of a mixture of Eulerian and Lagrangian variables, which are correlated by an interaction equation involving the Dirac

delta function. The Cartesian variables are defined on an underlying Cartesian mesh, on top of which a curvilinear mesh where the Lagrangian variables are defined moves freely. The evolutions of complex boundary geometries are essentially described by the movement of the curvilinear Lagrangian meshes. However, the numerical approximation of the Dirac function introduces an artificial transition layer in the vicinity of the boundary, which may cause volume loss of small structures, such as, blood vessels. It should be emphasized that a prominent advantage of using IBM for cardiac simulations is its simplicity of coupling the voltage propagation and the mechanical contractions of the heart, which makes it attractive in large scale simulations where the interactions of the surrounding tissue and heart plays an indispensable role.

The standard approach in cardiac simulations involving complex geometries is the finite volume method (FEM). This method has been successfully applied to the study of a wide range of topics in cardiology, including influence of abrupt changes in tissue geometry [45], unidirectional block due to wavefront curvature [91], blood flow around complex endovascular devices [11], and effects of coronary vasculature on defibrillation [8]. One of the most important advantages of FEM is its complete ecosystem. Since its invention in 1950s, FEM has become the most popular method in numerical solutions of partial differential equations, where complex geometries need to be handled. As a result, numerous commercial and open-source FEM packages have been developed for a variety of specific fields, such as, aerodynamics [113], fluid mechanics [15], thermodynamics [48], and magnetohydrodynamics [92]. It is worth noting, combined with high-quality mesh generating algorithms, FEM can accurately resolve fine anatomical structures, such as coronary vasculatures within ventricles. However, the generation of high-quality meshes is not trivial, in general several mesh generation procedures need to be inspected before the appropriate one is chosen, which

may incur a cost in both human- and machine-time.

Both IBM and FEM require an explicit handling of boundary conditions, which leads to relatively complicated code implementations near boundaries. To eliminate this complication, the phase-field method (PFM) has been introduced, in which boundary conditions are substituted by a partial differential equation for the evolution of an auxiliary phase-field [54]. Integral phase-field values zero and one are initially assigned to each mesh cell, with a transition occurs near the boundary. Then these integral values are diffused and the discrete boundary is defined to the collection of mesh cells where phase-field values are within the neighbourhood of a certain fractional. Since the explicit boundary conditions are eliminated, the implement of PFM can be much simpler than those of IBM and FEM. However, the diffused phase-field values introduced an artificial transition layer, which can lead to volume loss of the heart tissue and even total disappearance of fine structures [5]. Recently PFM is employed by Fenton et al. for the simulation of electrical scroll wave propagation in anatomically realistic rabbit ventricular models.

Another numerical method widely used in electrocardiac simulations is the finite volume method (FVM). In this method, the complex geometry of heart tissue is embedded in a Cartesian grid, where control volumes are defined as the intersections of Cartesian mesh cells and the tissue region. For each control volume, the divergence theorem is applied, which transform volume integrals into surface integrals. FVM has been successfully applied to the studies of extracellular potential distributions [83], cardiac ischaemia modelling [51], discontinuous electrical activations [102], etc. Unlike PFM, the domain boundaries are resolved accurately by the introduction of cut-cells, which makes it especially attracting when fine anatomical structures are involved. However, the extra accuracy does not come for free, since the handling of boundary conditions is

more complicated than for PFM. It is worth noting, the embedded boundary method (EBM) employed in this thesis is a modification of the original FVM. While the original FVM defines unknown variables at the centroids of control volumes, EBM always defines the unknowns at the centers of regular Cartesian cells [50]. The details of EBM will be elaborated in the following chapters.

1.3 Dissertation Organization

Chapter 1 gives a brief overview of the different mathematical models in electrocardiology and motivated the development of our new sharp boundary numerical method for simulating the action potential propagation in the cardiac tissue.

Chapter 2 presents the governing equations in the bidomain and monodomain model of electrocardiology and discusses the relations between this two commonly adopted models.

Chapter 3 introduces the expended embedded boundary (EBM) method. The treatment of the expended EBM follows ideas of [71, 108]. We present what appears to be a new feature for this method, the solution with anisotropic diffusion. Our solution is shown to be second-order accurate in the L_∞ (as well as the L_1) norm. Use of the L_∞ norm for convergence analysis means that the order of accuracy is maintained uniformly up to the boundary.

Chapter 4 is devoted to the verification of our method. We show the second-order convergence of the solution for the Poisson equation in a 3D spherical domain. And code comparison are made with the previously verified and validated phase field code [30].

Chapter 5 illustrated some of the applications of the new method in electrocardiac simulations. we illustrate the resolution of the method by showing the flow of electrical signals around small blood vessels, and for the bidomain model, the enhanced coupling between the two voltage systems that results. We illustrate the use of our code to determine (a) the smallest blood vessels relevant to defibrillation and (b) the coarsest grid to be used to study such small blood vessels. Depending on the purpose of the simulation and of the resulting accuracy required, the grid resolution needed will be determined. A detailed analysis of this nature is out of the scope of this thesis, as it depends on details not considered here (blood vessel wall resistivity, the physiology of small blood vessels in the heart, and the accuracy needed for the repeated simulations which will be part of a V&V, optimization, UQ and QMU analysis with engineering safety margins). In a separate study, the smallest relevant blood vessels have a diameter set by the blood vessel wall resistivity, and have been estimated as $200 \mu\text{m}$ [8]. From this fact and the present work, see especially the key Fig. 5.4, we require about 4 cells across the blood vessel. Thus we see that the maximum useful mesh size is about $200/4 = 50 \mu\text{m}$. This is to be compared to the heart itself, with a diameter of 8 cm [88].

Chapter 6 contains our main conclusions and a discussion of some promising improvements and extensions.

Chapter 2

Governing Equations

Electrocardiac physiology is described by a system of reaction-diffusion equations, with the transmembrane ionic currents defining the reaction and the electric potential equations solved as a diffusion process. Both the currents and the potentials represent averages over a region containing many cells. The problem is complicated by

- complex, stiff and interacting reaction rates
- thin walls of the quasi-two dimensional heart chamber with small scale features such as blood vessels or isolated regions of diseased tissue and
- strongly anisotropic diffusion, with more rapid diffusion along one dimensional fibres nearly parallel to the heart chamber walls.

In this chapter, we make a detailed description of the bidomain and monodomain models and show their relationship with each other. Then we discuss different types of ionic current models, which are necessary components in both the bidomain and

monodomain models. Through comparison with other ionic current models, we show that the Fenton-Karma (FK) model is both very efficient and accurate. As a result, we used the FK model in all the subsequent simulations of this thesis.

2.1 Bidomain Model

As reviewed in Chapter 1, there are two main categories of mathematical models describing the action potential propagation in the cardiac tissue: discrete models and continuous models. Although the restriction of computational resources in the earlier times made the discrete models more popular, with the recent fast development of high performance computing clusters (HPCC) [55], the continuous models have become the standard choice of the electrocardiologist community, for their allowance of continuously varying myocyte states.

To the date, the most complete and widely adopted continuous model of electrical activities within the heart is the bidomain model. In this model, the unequal anisotropy ratios of the intracellular and extracellular spaces are expressed explicitly, which better reflects the fact, compared with the simplistic monodomain model (discussed in the next section), that myocytes are embedded in a complex network of gap junctions, body fluid and fine capillaries, etc. As the defibrillation voltage is deposited in the extracellular tissue, but its beneficial effect occurs within the cellular tissue, the bidomain model, which couples the two is needed for defibrillation studies.

2.1.1 Model Equations

In the most general case, the bidomain model describes the distribution of electrical potential in a domain Ω , which consists of the heart tissue region \mathbb{H} , and the surrounding tissue region $\mathbb{T} = \Omega \setminus \mathbb{H}$. It is assumed that \mathbb{H} is a syncytium composed of overlapping intracellular and extracellular spaces, which are coupled with each other by transmembrane current flows [16]. To make the following discussions more clear, we introduce some notations here. We use ϕ_i and ϕ_e to denote the intracellular and extracellular potentials, respectively. And the electric potential in the surrounding tissue \mathbb{T} is denoted by ϕ_t . Besides, C_m denotes the membrane capacity and χ denotes the surface to volume ratio of the cardiac myocytes.

D_i , D_e and D_t are defined as the anisotropic conductivity tensors in the intracellular, extracellular, and surrounding tissue regions, respectively. The elements of D_i and D_e are determined by the local myocardial fibre orientation [31],

$$D_* = \beta_*^\perp \mathbf{I} + (\beta_*^\parallel - \beta_*^\perp) \mathbf{f}\mathbf{f}^T, \quad (2.1)$$

where β_*^\parallel and β_*^\perp (*=i, e), are the conductivities longitudinal and transversal to the fibre, which is parallel to a unit vector \mathbf{f} . As in [24], we assume D_t to be an isotropic tensor,

$$D_t = \beta_t \mathbf{I}, \quad (2.2)$$

where β_t is the scalar conductivity in \mathbb{T} .

By Ohm's law, we get the current densities J_i and J_e in the intracellular and extracellular spaces, respectively:

$$J_i = -D_i \nabla \phi_i, \quad (2.3)$$

$$J_e = -D_e \nabla \phi_e. \quad (2.4)$$

By assuming only membrane related sources in the intracellular and extracellular spaces, the law of the conservation of electric charges leads to the following divergence forms:

$$\nabla \cdot J_i = -I_m, \quad (2.5)$$

$$\nabla \cdot J_e = I_m, \quad (2.6)$$

where I_m is the transmembrane current term, which assumes the following form

$$I_m = \chi \left(C_m \frac{\partial \phi}{\partial t} + I_{\text{ion}}(\phi, \mathbf{y}) \right). \quad (2.7)$$

In Eq. 2.7, $\phi = \phi_i - \phi_e$ is the transmembrane voltage, and $I_{\text{ion}}(\phi, \mathbf{y})$ corresponds to the ionic current component, which is determined by ϕ and the vector of gate variables \mathbf{y} controlling the ionic current channels in the membrane. It is worth noting that there are a lot of different models describing the dynamics of the gate variable \mathbf{y} , which are systems of ordinary differential equations (ODE) as following,

$$\frac{\partial \mathbf{y}}{\partial t} = g(\phi, \mathbf{y}). \quad (2.8)$$

These ODE models varies greatly in their complexity, from the simplest FitzHugh-Nagumo model [79] with only two gate variables, to the very complex Iyer-Mazhari-Winslow model [104] with as many as 67 variables. In this thesis, we will adopt the Fenton-Karma (FK) model, which is both computationally efficient and flexible enough to match the results from more complex models and experiments. In the FK model

$$I_{\text{ion}}(\phi, \mathbf{y}) = I_{\text{fi}}(\phi, v) + I_{\text{so}}(\phi) + I_{\text{si}}(\phi, w), \quad (2.9)$$

$$\frac{\partial v}{\partial t} = H(\phi_c - \phi)(1 - v)/\tau_v^- - H(\phi - \phi_c)v/\tau_v^+, \quad (2.10)$$

$$\frac{\partial w}{\partial t} = H(\phi_c - \phi)(1 - w)/\tau_w^- - H(\phi - \phi_c)w/\tau_w^+, \quad (2.11)$$

$$I_{\text{fi}}(\phi, v) = -\frac{v}{\tau_d}H(\phi - \phi_c)(1 - \phi)(\phi - \phi_c), \quad (2.12)$$

$$I_{\text{so}}(\phi) = \frac{\phi}{\tau_o}H(\phi_c - \phi) + \frac{1}{\tau_r}H(\phi - \phi_c), \quad (2.13)$$

$$I_{\text{si}}(\phi, w) = -\frac{w}{2\tau_{\text{si}}}(1 + \tanh[k(\phi - \phi_c^{\text{si}})]), \quad (2.14)$$

where I_{fi} , I_{so} and I_{si} denote the fast-inward, slow-outward, and slow-inward ionic currents respectively, $\mathbf{y} = (v, w)$ is the vector of gate variables controlling the fast- and slow-inward components, and H is the standard Heaviside step function. A detailed discussion of the FK model and the values of parameters in it can be found in [32].

Combining Eqs. 2.3, 2.5, and 2.7, we get the parabolic part of the bidomain differential equations system

$$\nabla \cdot (D_i \nabla (\phi + \phi_e)) = \chi \left(C_m \frac{\partial \phi}{\partial t} + I_{\text{ion}}(\phi, \mathbf{y}) \right). \quad (2.15)$$

On the other hand, adding Eq. 2.5 to Eq. 2.6 gives

$$\nabla \cdot (J_i + J_e) = 0. \quad (2.16)$$

Substitute Eqs. 2.3 and 2.4 and the relation $\phi_i = \phi + \phi_e$ into Eq. 2.16, we get

$$\nabla \cdot (D_i \nabla \phi) + \nabla \cdot ((D_i + D_e) \nabla \phi_e) = 0, \quad (2.17)$$

which is one of the elliptic equations in the bidomain model. Similarly, we can apply the conservation law of electric charges to the surrounding region \mathbb{T} , which leads to the other elliptic equation in the bidomain model:

$$\nabla \cdot (D_t \nabla \phi_t) = 0. \quad (2.18)$$

2.1.2 Boundary Conditions

As any other differential systems, the existence and uniqueness of the solution to the bidomain model depends on the specification of the proper boundary conditions. As a convention for notations, we use $\partial\mathbb{H}$ to denote the boundary of the cardiac tissue,

and $\partial\mathbb{T}$ to denote the exterior boundary of the surrounding tissue (in contrast, the interior boundary is adjacent to \mathbb{H}). We assume the surrounding tissue is electrically isolated from the environment, then there is no current through $\partial\mathbb{T}$, which gives

$$D_t \nabla \phi_t \cdot \mathbf{n} = 0, \quad (2.19)$$

where \mathbf{n} is the unit normal vector on $\partial\mathbb{T}$. On the boundary of cardiac tissue $\partial\mathbb{H}$, a common assumption [4] is that there exists direct contact between the extracellular space of \mathbb{H} and the surrounding tissue \mathbb{T} , which leads to the continuation of the potential

$$\phi_e = \phi_t, \quad (2.20)$$

and the current

$$D_e \nabla \phi_e \cdot \mathbf{n} = D_t \nabla \phi_t \cdot \mathbf{n}. \quad (2.21)$$

Lastly, we assume there is an isolation between the intracellular space of \mathbb{H} and the surrounding tissue \mathbb{T} , which leads to

$$D_i \nabla \phi_i \cdot \mathbf{n} = 0,$$

which is equivalent to

$$D_i \nabla \phi \cdot \mathbf{n} + D_e \nabla \phi_e \cdot \mathbf{n} = 0. \quad (2.22)$$

For convenience considerations, we collect all the differential equations (Eqs. 2.8, 2.15, 2.17, 2.18) and the boundary conditions (Eqs. 2.19, 2.20, 2.21, 2.22) of the bidomain model, and list here

$$\nabla \cdot (D_i \nabla \phi) + \nabla \cdot (D_i \nabla \phi_e) = \chi \left(C_m \frac{\partial \phi}{\partial t} + I_{\text{ion}}(\phi, \mathbf{y}) \right) \quad \mathbf{x} \in \mathbb{H}, \quad (2.23)$$

$$\nabla \cdot (D_i \nabla \phi) + \nabla \cdot ((D_i + D_e) \nabla \phi_e) = 0 \quad \mathbf{x} \in \mathbb{H}, \quad (2.24)$$

$$\frac{\partial \mathbf{y}}{\partial t} = g(\phi, \mathbf{y}) \quad \mathbf{x} \in \mathbb{H}, \quad (2.25)$$

$$\nabla \cdot (D_t \nabla \phi_t) = 0 \quad \mathbf{x} \in \mathbb{T}, \quad (2.26)$$

$$\phi_e - \phi_t = 0 \quad \mathbf{x} \in \partial \mathbb{H}, \quad (2.27)$$

$$D_e \nabla \phi_e \cdot \mathbf{n} - D_t \nabla \phi_t \cdot \mathbf{n} = 0 \quad \mathbf{x} \in \partial \mathbb{H}, \quad (2.28)$$

$$D_i \nabla \phi \cdot \mathbf{n} + D_i \nabla \phi_e \cdot \mathbf{n} = 0 \quad \mathbf{x} \in \partial \mathbb{H}, \quad (2.29)$$

$$D_t \nabla \phi_t \cdot \mathbf{n} = 0 \quad \mathbf{x} \in \partial \mathbb{T}, \quad (2.30)$$

to which we will apply our extended embedded boundary method for numerical simulations.

2.2 Monodomain Model

Although the bidomain is the most complete description of the electrical phenomena occurring within the cardiac tissue, it is difficult to design both efficient and accurate numerical schemes for it. However, if we assume there is no injection of current into the extracellular space, it can be simplified to the monodomain model, which can generate highly accuracy approximations to the original bidomain model [90]. In

contrast to the bidomain model, the monodomain model only involves a single PDE, which is numerically more tractable.

The key simplifying assumption is that the anisotropy of the intracellular space is the same as that of the extracellular space, which is equivalent to the statement that the intracellular diffusion tensor D_i is proportional to the extracellular diffusion tensor D_e ,

$$D_i = \alpha D_e. \quad (2.31)$$

Substitute Eq. 2.31 into Eqs. 2.23, 2.24, we get

$$\nabla \cdot \left(\frac{1}{1+\alpha} D_i \nabla \phi \right) = \chi \left(C_m \frac{\partial \phi}{\partial t} + I_{\text{ion}}(\phi, \mathbf{y}) \right).$$

By defining $D = \frac{D_i}{(1+\alpha)\chi C_m}$, the above equation is simplified into

$$\frac{\partial \phi}{\partial t} = \nabla \cdot (D \nabla \phi) - \frac{\nabla \cdot (D_i \nabla \phi)}{C_m}, \quad (2.32)$$

which is the common form of the monodomain equation. It should be emphasized that the solution domain of the monodomain model only includes the cardiac tissue region \mathbb{H} , so we only need to specify the boundary condition on $\partial\mathbb{H}$. Following the convention in most cardiological literatures, we assume the heart tissue is electrically isolated from the environment, which leads to the non-flux boundary condition

$$D \nabla \phi \cdot \mathbf{n} = 0. \quad (2.33)$$

Chapter 3

Numerical Methods

3.1 Overview of Numerical Methods

The goal of the present work is to resolve small features within the diffusion equation on computationally feasible grids. At issue is the number of grid cells needed to obtain convergence relative to the fine scale feature size. Additionally, the sharp boundaries (of the heart tissue or of the feature) are a numerical issue, so that localized convergence near the heart boundary or near a feature is an important issue.

We mention commonly used methods for the solution of the diffusion equation, but a full comparison of these methods is out of the scope of the present paper.

3.1.1 Ghost Cell Method

Ghost Cell (GC) [17, 56]. The ghost cell method was originally developed to solve fluid dynamics problems where internal boundaries play an important role

[42]. This method has been adopted extensively for its great capability to track discontinuities as sharp internal boundaries and conserve the conserved quantities at a discrete level [42]. This method has been used to implement highly accurate boundary conditions for both body-fitted grids and Cartesian grids [20].

The underlying idea of the ghost cell method is very straightforward. Missing data points near a domain boundary for a finite difference stencil used to solve the differential equation are added by extrapolation from interior points along coordinate directions, even ambiguously if needed in higher dimensions near concave boundary segments. In effect, this plan is equivalent (or nearly so) to a stair step interface, located at the cell edges that mark a transition from a cell center which lies in the domain to a cell center outside of the domain.

Compared with body-fitted grid computations, e.g., the finite element method, the ghost cell method doesn't incur the costly grid-generation expenses. And it has been shown in simulations of compressible flow about circular cylinders and airfoil applications [21], that the ghost cell method can achieve the same high accuracy as more complex body-fitted method. However, most of the traditional implementations of the ghost cell method suffers from the shortcoming that grid clustering near the body must be maintained to the far-field boundary [82]. To overcome this problem, a type of local mesh refinement [26] has been proposed for resolving the vicinity of boundaries in structured grids.

The original reference is first order [42], but extensions to second order accuracy have been given [40].

3.1.2 Phase Field Method

Phase Field (PF) [31]. The phase field method has been applied to a wide range of problems including thermodynamics [84], material solidification [54], melt convection [5], and intracellular dynamics [59]. As with the level set method [78], the main advantage of the phase field method is its avoidance of the explicit track of interfaces.

An additional equation (the phase field) interpolates between the inside and the outside, with a diffusive interface connecting these two regions. The width of the interface zone depends on the particular choice of the phase field function, and the typical value is five cells [31]. This method is only first order accurate, which means a relatively high computational overhead when simulations with fine resolution are performed. In [10] the phase field width is reduced to zero in a mathematical limit, leading to a thin or thinner interface transition region. The method appears to be first order accurate (when a sharp interface is specified as input), but the order of convergence has not been documented.

It is worth noting that the phase field method has been applied by Fenton et al. [31] to the simulations of electrical wave propagation in cardiac tissue with none trivial geometries. As a way to verify the correctness of our new sharp boundary embedded boundary method, we perform a comparison study in Chap 4 with the phase field method, where the transmembrane potential (V) and the conduction velocity (CV) are simulated using both method. The final results shows V and CV converges to the common asymptotic values with mesh refinement for both method.

3.1.3 Immersed Boundary Method

Immersed Boundary Method (IBM) [86, 73]. The immersed boundary method was first developed by Peskin [85] for the simulation of cardiac mechanics and associated blood flow. Later numerous variations of the original immersed boundary method have been proposed and applied to the simulations of inviscid flows with complex immersed boundaries [2] and unsteady viscous flows [105].

The underlying idea of the immersed boundary method is similar to that of the phase field method, which is the avoidance of the creation of structured or unstructured grids that conform to the body. In traditional finite volume or finite element method, a two step process is needed for the generation of structured or unstructured grids. In the first step, a surface grid covering the boundaries is generated. Then the surface grid is adopted as the boundary condition for the generation of the body grid for the volume enclosed by the surface. Once the grid is generated, the transformation to a curvilinear coordinate system is introduced, and the original PDE systems can be solved using the conventional finite difference method. However, in many situations, the cost for generating fine quality surface and volume grids is very high, which greatly decrease the efficiency and applicability of the traditional method.

On the contrary, the task of grid generation in the immersed boundary method is greatly simplified. This is especially true for the simulations of flows with moving boundaries, in which the traditional methods need to generate a body-conformal grid for every time step [80]. In contrast, in the immersed boundary method, the Heaviside function associated with the boundary is replaced with a numerically spread Heaviside function. Only one Cartesian grid is generated for the whole simulation. However, the complexity reduction comes with the expense of a more complex treatment of the

boundary conditions. This feature is typical for Cartesian type methods, such as the embedded boundary method, which is discussed in subsequent sections. In general, the interface width of the immersed boundary method is several cells wide, with the width depending on the size of the jump in the coefficients. The method and its accuracy is well documented. It is first order accurate.

3.1.4 Finite Element Method

Finite Elements [91]. Arguably the finite element method is the most popular method used in both industrial and academic investigations where domains with complex geometries are involved. It has been successfully used in a vast range of practical projects including thermodynamics [60], solid mechanics [44], aerodynamics [37], electromagnetism [39], environment protection [72], and nanotechnology [89]. The widely acceptance of the finite elements comes from its solid mathematical foundation, extreme versatile applicability, and relatively straight underlying ideas. Moreover, the great availability of the finite element implementations in commercial and open source libraries has made it particularly popular in the simulation of the behaviours of complex physical systems, and the design phase of large engineering projects [22].

The method requires a body-fitting grid adapted to complex problem features. The whole problem domain is subdivided into simpler parts, which is called finite elements. Then the solution of the partial differential equations describing the underlying mechanics of the physical or engineering system will be transformed to a collection of variational problems, the minimal solutions of which are solved on each finite element. The combination of these solutions will give an approximation to the original problem to an order of accuracy determined by the specification of the simulation task and

the computational resources available. It should be pointed out that, the generation of the finite elements and the process of combining numerical solutions on each finite element to construct global approximation demands a lot of computational efforts, in the sense of both developing time and computational time [99], which is in contrast to the methods where a body-fitting mesh is not necessary, such as, the phase field method, immersed boundary method, and the embedded boundary method.

3.1.5 Immersed Interface Method

Immersed Interface Method (IIM) [65]. The immersed interface method was originally proposed to numerically solve flow problems where the interaction between the flow and moving boundaries play an important role in the underlying mechanics [61]. The main motivation for the invention of the immersed interface method is similar to those of the other Cartesian grid methods, such as, the immersed boundary method and the embedded boundary method, which is to avoid the cost of constantly reconstruct body-fitting grid for moving boundary problems.

To clearly explain the idea underlying the immersed interface method, we need to have a better understanding of the aforementioned immersed boundary method [85]. In the original immersed boundary method, the boundary of the immersed object is treated as a collection of Lagrangian particles, the configuration of which determines the distribution of the force resulted by the existence of the object on the immersing fluid. These Lagrangian boundary is immersed in a Cartesian grid representing the fluid, and a Dirac delta function is introduced to approximate the interaction between the boundary and the fluid. The coupling between the immersed boundary and the fluid field is through the spreading of the singular force, represented by the Dirac function,

from the Lagrangian boundary to the Cartesian mesh, and the feedback of the fluid velocity in the other way around [111]. The adoption of the Dirac function successfully removes the singularity in the partial differential equations and the underlying fluid field, which greatly simplifies the formulation of the numerical schemes. However, the simplicity doesn't come without any cost, one major shortcoming of the immersed boundary method is the introduction of an artificial thickness resulted by the utilization of discrete Dirac functions. As a result, lots of effort has been devoted to find optimal discrete Dirac functions with a narrow support [87].

The major shortcoming of the original immersed boundary method is that it is only first order accuracy [85]. To overcome this shortcoming the immersed interface method was proposed by LeVeque and Li [64]. The most important difference between this method and the immersed boundary method is that, the new method explicitly incorporates the jump condition resulted from the existence of the Dirac function into the finite difference method [63]. The elimination of the requirement that the Dirac function to be approximated by a smooth function, which leads to sharp immersed boundaries and overall second order accuracy. One prominent advantage of the immersed interface method over the immersed boundary method is that, when all the necessary jump conditions are known, the sharpness of the boundary computed by the method doesn't depend on the grid resolution, which means second or even higher order accuracy can be achieved [111]. Another advantage is that the immersed interface method conserves the volume enclosed by the immersed boundary very well, which makes it attractive to model conservation laws.

However, the high order immersed interface method requires the derivation of necessary jump conditions across the boundary, a process which is not at all straight forward or intuitive. The resulting implementation is sometimes complicated and the

the addition of additional degrees of freedom within the cut cells will also increase the computing overhead [61].

3.1.6 Embedded Boundary Method

Embedded Boundary Method (EBM) [71, 108]. The embedded boundary method is also a Cartesian grid method. It is originally developed to solve single component Poisson [50] and heat equations [71] in 2D domain with complex geometries, and has been extended to handle problems in 3D domains [94] and with multiple components [106]. The method is able to achieve second order convergence and doesn't require the specification of complicated geometries as the immersed interface method. In essence, the embedded boundary method is a type of finite volume method, so the high order flux integration over boundary faces in cut cells plays an important role in the overall accuracy of the method.

It is worth noting that the original embedded boundary method is only able to handle elliptic operators with isotropic diffusion tensor, which is a too strong requirement for modelling the electrocardiac phenomena, where the existence of fibre orientations, inter-cellular junctions and sick tissues [95] all contribute do the anisotropic properties of the cardiac tissue. To overcome this shortcoming, here we present an extended sharp boundary embedded boundary method, which is specifically designed to handle anisotropic elliptic operators. It has second order convergence in L_∞ (uniformly up to the boundary), so that boundary region anomalies will not occur in the solution. And the details of the new algorithm is given in the following section.

3.2 Embeded Boundary Method

On the basis of the above survey, the EBM (and possibly also IIM) appear to be the most suitable for high resolution of fine detailed features in the heart geometry, with blood vessels and/or defective tissues defining the fine scale structures.

We use the EBM to discretise the parabolic subsystem of the FK model. Originally proposed by Colella et al. [50, 71, 94], the EBM method maintains sharp boundaries and interfaces in geometrically complex domains [93, 108]. It is locally conservative and robust in marginally resolved calculations [94]. The EBM has recently been extended to solve the elliptic interface problem [19, 93, 108] and the two-phase incompressible flow problem [107].

EBM is a finite difference method, which treats cut cells (grid cells partly inside the cardiac tissue and partly outside) in a manner differently from the regular, non-cut cells. The computational domain is thus discretized as a collection of control volumes formed by the intersection of the domain with rectangular Cartesian grid cells. Whether a cell center is inside or outside of the domain, the corresponding primary unknowns are always cell-centered.

To achieve accurate solutions of the voltage equation, additional degrees of freedom are needed for the cut cells. It is necessary to capture the crossings of the cardiac anatomy with the underlying Cartesian grids to apply the EBM. This geometrical information is readily available in most state-of-art mesh generation tools and we adopt the FrontTier library [41]. The diffusion process in a cut cell has zero values in the outside portion of the cut cell and "normal" values in the interior portion of the cut cell. Thus the tensor diffusivities defined in the interior region must be supplemented by information on the size of the interior and exterior portions of the cut cell. With

tensor, as opposed to scalar diffusivities, directives of the voltage in x-, y-, and z-direction, instead of only the derivative normal to the tissue boundary, are involved in the calculation of boundary flux.

The result, as analysed in [71] is a second order accurate method in the L_∞ norm, meaning that anomalous boundary signals will not occur in the method. This result is established for a scalar diffusion matrix only, and the cited reference explains the method in this case only. Accordingly, we detail here the discretization and the modifications needed for a tensor diffusivity, and document in Chap. 4 convergence rates for this case, a new contribution of the present paper. The algorithm is organized in a manner that allows formulation for an arbitrary order of accuracy.

To solve the non-linear system of equations in the bi-domain model numerically, we adopt the operator splitting scheme proposed by Dos Santos et al [24]. In this discretization, each time step consists of the solution of three sub-problems, i.e., a parabolic PDE, a system of non-linear ODEs, and a system of elliptic PDEs. The second order Crank-Nicolson method and first order forward-Euler method are used to solve the parabolic PDE and the system of non-linear ODEs respectively, which leads to the following semi-discrete system:

$$1. \quad \left(1 - \frac{\Delta t}{2} L_i\right) \varphi^{n+1/2} = \left(1 + \frac{\Delta t}{2} L_i\right) \varphi^n + \Delta t L_i \varphi_e^n, \quad (3.1)$$

$$2. \quad \varphi^{n+1} = \varphi^{n+1/2} - \Delta t I_{\text{ion}}(\varphi^{n+1/2}, y^n) / (\chi C_m), \quad (3.2)$$

$$y^{n+1} = y^n + \Delta t g(\varphi^{n+1/2}, y^n), \quad (3.3)$$

$$3. \quad (L_i + L_e) \varphi_e^{n+1} = -L_i \varphi^{n+1}, \quad (3.4)$$

$$L_t \varphi_t^{n+1} = 0, \quad (3.5)$$

where L_i , L_e and L_t denote the operators $\nabla \cdot (D_i \nabla) / (\chi C_m)$, $\nabla \cdot (D_e \nabla) / (\chi C_m)$, and $\nabla \cdot (D_t \nabla)$; φ^{n+1} , φ_e^{n+1} , φ_t^{n+1} , and y^n are discretizations of ϕ , ϕ_e , ϕ_t , and y at time step n . The von Neumann analysis in [50] shows the above scheme is unconditionally stable.

The EBM method is applied to solve the parabolic PDE (3.1) and the system of elliptic PDEs (3.4, 3.5) in the above semi-discrete system. To give a clear explanation of the EBM method, it is necessary to make a mathematically unambiguous description of the spatial discretization of the solution domain. We will follow the notations given by Schwartz et al. [94], describing the discretization of a general irregular domain Ω embedded in a Cartesian grid. The Cartesian grid consists of rectangular cuboids $\Gamma_{\mathbf{i}} = [\mathbf{i}h, (\mathbf{i} + \mathbf{u})h]$, $\mathbf{i} \in \mathbb{Z}^3$, where \mathbf{u} is the vector with all entries equal to one, h is the mesh spacing. We define control volumes $V_{\mathbf{i}} = \Gamma_{\mathbf{i}} \cap \Omega$ and face elements $A_{\mathbf{i} \pm \frac{1}{2} \mathbf{e}_d}$, which is the intersection of $\partial V_{\mathbf{i}}$ with the coordinate planes $\{\mathbf{x} : x_d = (i_d \pm \frac{1}{2})h\}$. Here \mathbf{e}_s is the unit vector in the s -direction. Similarly we define the boundary elements $A_{\mathbf{i}}^B$ to be $\partial \Omega \cap \Gamma_{\mathbf{i}}$. Then we have the following decomposition of the surfaces of control volumes:

$$\partial V_{\mathbf{i}} = \left(\bigcup_{s=1}^d A_{\mathbf{i} \pm \frac{1}{2} \mathbf{e}_s} \right) \cup A_{\mathbf{i}}^B.$$

With the above definitions of the basic geometric objects, several real-valued quantities necessary for the EBM discretization can be introduced.

- Dimensionless area: volume fractions $\kappa_{\mathbf{i}} = |V_{\mathbf{i}}| h^{-d}$, face apertures $\alpha_{\mathbf{i} \pm \frac{1}{2} \mathbf{e}_s} = |A_{\mathbf{i} \pm \frac{1}{2} \mathbf{e}_s}| h^{-(d-1)}$, and boundary apertures $\alpha_{\mathbf{i}}^B = |A_{\mathbf{i}}^B| h^{-(d-1)}$.
- Centroids and average outward normals to the boundary

$$\mathbf{x}_i = \frac{1}{|V_i|} \int_{V_i} \mathbf{x} dV,$$

$$\mathbf{x}_{i \pm \frac{1}{2} e_s} = \frac{1}{|A_{i \pm \frac{1}{2} e_s}|} \int_{A_{i \pm \frac{1}{2} e_s}} \mathbf{x} dA,$$

$$\mathbf{x}_i^B = \frac{1}{|A_i^B|} \int_{A_i^B} \mathbf{x} dA,$$

$$\mathbf{n}_i^B = \frac{1}{|A_i^B|} \int_{A_i^B} \mathbf{n} dA,$$

where \mathbf{n}^B is the outward normal to $\partial\Omega$. To achieve second or higher order accurate numerical method, a way to approximate the above geometric quantities is needed. Here we employ the marching tetrahedra method [101], a widely used algorithm in computer graphics for generating implicit surfaces, which clarifies eliminate some ambiguity problems of the well known marching cubes algorithm [67]. To avoid disturbance to the description to the main algorithm, the details of using the marching tetrahedra method to calculate the aforementioned geometric quantities is deferred to Sec.

Since the EBM method discussed here can be used to solve a variety of elliptic and parabolic PDEs, we will illustrate the detailed scheme in a more general way than the specific application for the bi-domain model. The main innovation of the new scheme is in the discretization of the flux through surfaces of each control volume. We apply the EBM method to the Poisson equation with the Dirichlet boundary condition

$$\nabla \cdot D \nabla \psi = \rho, \text{ in } \Omega \quad (3.6)$$

$$D \nabla \psi = g_d(\mathbf{x}), \text{ on } \partial \Omega \quad (3.7)$$

where D is an anisotropic diffusion tensor. Brief discussions indicating the construction of high order schemes to parabolic equations and Neumann boundary conditions will be given later.

In the EBM method, we average Eq. (3.6) over each control volume Γ_i , and use the divergence theorem to transform the volume integrals into integrals over the boundary $\partial \Gamma_i$

$$\int_{V_i} \rho dV = \sum_{\pm=+,-} \sum_{s=1}^d \int_{A_{i \pm \frac{1}{2} \mathbf{e}_s}} \vec{F} \cdot \mathbf{n} dA + \int_{A_i^B} \vec{F} \cdot \mathbf{n} dA, \quad (3.8)$$

where the flux term $\vec{F} = D \nabla \psi$. As in [18], we define the notation $\langle \cdot \rangle_{\mathbb{S}}$ as the average of a quantity over the domain \mathbb{S} (2D or 3D), then Eq. (3.8) can be rewritten as

$$\langle \rho \rangle_i = \frac{1}{\kappa_i h} \left(\sum_{\pm} \sum_s \alpha_{i \pm \frac{1}{2} \mathbf{e}_s} \langle \vec{F} \cdot \mathbf{n} \rangle_{i \pm \frac{1}{2} \mathbf{e}_s} + \alpha_i^B \langle \vec{F} \cdot \mathbf{n} \rangle_{i,B} \right), \quad (3.9)$$

where the further notation simplifications $\langle \cdot \rangle_i = \langle \cdot \rangle_{V_i}$, $\langle \cdot \rangle_{i \pm \frac{1}{2} \mathbf{e}_s} = \langle \cdot \rangle_{A_{i \pm \frac{1}{2} \mathbf{e}_s}}$, and $\langle \cdot \rangle_{i,B} = \langle \cdot \rangle_{A_i^B}$ are introduced. A variety of high order schemes can be introduced by applying appropriate quadrature rules to the calculation of average values in Eq. (3.9). At a first glance, a n th order quadrature rule over V_i and $(n+1)$ th order quadrature

rules over $A_{i\pm\frac{1}{2}\mathbf{e}_s}$ and A_i^B are necessary for the construction of n th order accurate finite volume schemes for Eq. (3.9). However, a modified equation analysis as in [50] shows that approximating $\langle \vec{F} \cdot \mathbf{n} \rangle_{i\pm\frac{1}{2}\mathbf{e}_s}$ and $\langle \vec{F} \cdot \mathbf{n} \rangle_{i,B}$ to the n th order of accuracy is sufficient to make the solution errors n th order convergent. For high order quadrature rules on irregular domains the reader can refer to [62, 112].

In the remaining part of the paper, we will focus on a 2nd order discretization of Eq. (3.9), which requires us to approximate both $\langle \vec{F} \cdot \mathbf{n} \rangle_{i\pm\frac{1}{2}\mathbf{e}_s}$ and $\langle \vec{F} \cdot \mathbf{n} \rangle_{i,B}$ to the 2nd order. It is easy to verify that

$$\langle \vec{F} \cdot \mathbf{n} \rangle_{i\pm\frac{1}{2}\mathbf{e}_s} = D(\mathbf{x}_{i\pm\frac{1}{2}\mathbf{e}_s}) \nabla \psi(\mathbf{x}_{i\pm\frac{1}{2}\mathbf{e}_s}) \cdot \mathbf{e}_s + O(h^2), \quad (3.10)$$

$$\langle \vec{F} \cdot \mathbf{n} \rangle_{i,B} = D(\mathbf{x}_i^B) \nabla \psi(\mathbf{x}_i^B) \cdot \mathbf{n}_i^B + O(h^2). \quad (3.11)$$

Since we assume the geometric quantities $\mathbf{x}_{i\pm\frac{1}{2}\mathbf{e}_s}$, \mathbf{x}_i^B , and \mathbf{n}_i^B are accurate to $O(h^2)$, second-order approximations to the gradient $\nabla \psi$ at the centroids $\mathbf{x}_{i\pm\frac{1}{2}\mathbf{e}_s}$ and \mathbf{x}_i^B suffices to make the whole scheme $O(h^2)$ accurate.

3.3 The Gradient Approximation at A Face Centroid

We define the discrete variable ϕ , $\phi_i \approx \psi((\mathbf{i} + \frac{1}{2}\mathbf{u})h)$. Then the gradient at the face centroids $\nabla \psi(\mathbf{x}_{i\pm\frac{1}{2}\mathbf{e}_s})$ can be approximated by linear combinations of ϕ_i and the boundary values. At any given face $A_{i\pm\frac{1}{2}\mathbf{e}_s}$, two types of approximations of ψ 's partial derivatives need to be constructed: $\phi'_{i\pm\frac{1}{2}\mathbf{e}_s} \approx \frac{d\psi}{d\mathbf{e}_s}(\mathbf{x}_{i\pm\frac{1}{2}\mathbf{e}_s})$, the derivative along the axis normal to the face; and $\phi'_{i\pm\frac{1}{2}\mathbf{e}_{s'}} \approx \frac{d\psi}{d\mathbf{e}_{s'}}(\mathbf{x}_{i\pm\frac{1}{2}\mathbf{e}_{s'}})$, $s' \neq s$, the derivatives along axes parallel to the face. We detail the numerical schemes used in each case.

3.3.1 Normal Derivative Approximation

In this case, we will follow the bilinear interpolation method in [94]. Firstly, centered differences in the normal direction are calculated at the centers of four faces including the face $A_{i \pm \frac{1}{2} e_s}$. Then iterated linear interpolations in the two axis-directions parallel to $A_{i \pm \frac{1}{2} e_s}$ are performed to get an $O(h^2)$ accurate derivative value at the face centroid. It should be emphasized that by “face center”, we refer to the center of the full rectangular face, which does not necessarily coincide with the face centroid $\mathbf{x}_{i \pm \frac{1}{2} e_s}$ calculated by quadrature rules.

As a concrete example, we consider the face $A_{i + \frac{1}{2} e_3}$ with outward normal \mathbf{e}_3 as shown in Fig 3.1, where \mathbf{p}_k ($k = 1 \dots 4$) are the face centers, and \mathbf{p} is the face centroid. To simplify the formulas, we introduce the following notation

$$\phi_{(l,m,n)}^i = \phi_{\mathbf{i} + l\mathbf{e}_1 + m\mathbf{e}_2 + n\mathbf{e}_3}. \quad (3.12)$$

Then we define $\phi_z^{\mathbf{p}_k}$ as the centered difference in the direction of \mathbf{e}_3 at the face center \mathbf{p}_k , i.e.

$$\phi_z^{\mathbf{p}_1} = \frac{\phi_{(0,0,1)}^i - \phi_{(0,0,0)}^i}{h}, \quad \phi_z^{\mathbf{p}_2} = \frac{\phi_{(1,0,1)}^i - \phi_{(1,0,0)}^i}{h}, \quad (3.13)$$

$$\phi_z^{\mathbf{p}_3} = \frac{\phi_{(1,1,1)}^i - \phi_{(1,1,0)}^i}{h}, \quad \phi_z^{\mathbf{p}_4} = \frac{\phi_{(0,1,1)}^i - \phi_{(0,1,0)}^i}{h}. \quad (3.14)$$

Lastly, we perform the bilinear interpolation

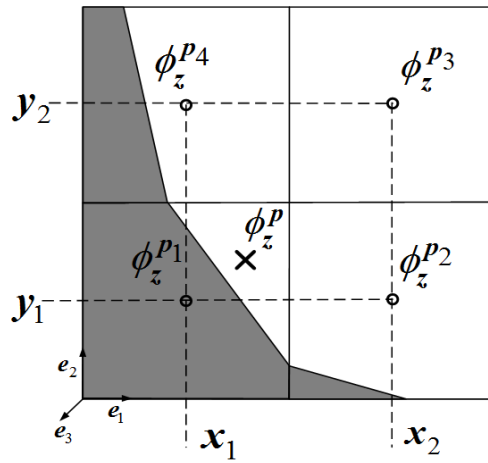


Figure 3.1: Stencil for the approximation of the normal derivative at the face centroid.

$$\phi_z^{\mathbf{p}} = \sum_{k=1}^4 \lambda_z^k \phi_z^{\mathbf{p}_k}, \quad (3.15)$$

where the interpolation coefficients are

$$\lambda_z^1 = \frac{(x - x_2)(y - y_2)}{(x_1 - x_2)(y_1 - y_2)}, \quad \lambda_z^2 = \frac{(x - x_1)(y - y_2)}{(x_2 - x_1)(y_1 - y_2)}, \quad (3.16)$$

$$\lambda_z^3 = \frac{(x - x_1)(y - y_1)}{(x_2 - x_1)(y_2 - y_1)}, \quad \lambda_z^4 = \frac{(x - x_2)(y - y_1)}{(x_1 - x_2)(y_2 - y_1)}. \quad (3.17)$$

3.3.2 Parallel Derivative Approximation

In this case, we start by calculating centered averages in the normal direction at the centers of nine faces including face $A_{i \pm \frac{1}{2} \mathbf{e}_s}$. Then we perform the bi-quadratic interpolation with the average values to get a quadratic polynomial in two variables. Finally, we calculate the partial derivatives of that polynomial and get their values at the face centroid $\mathbf{x}_{i \pm \frac{1}{2} \mathbf{e}_s}$. Since the centered average is accurate to $O(h^2)$, and the biquadratic interpolation is accurate to $O(h^3)$, the aforementioned scheme results in parallel derivative approximations accurate to $O(h^2)$.

Similar to the situation in Fig 3.1, we consider the example of a face $A_{i + \frac{1}{2} \mathbf{e}_3}$ with outward normal \mathbf{e}_3 as shown in Fig 3.2. As before, \mathbf{p}_k ($k = 1 \dots 9$) and \mathbf{p} are face centres and the face centroid, respectively. We fine $\bar{\phi}^{\mathbf{p}_k}$ as the centered average at the face center \mathbf{p}_k , i.e.,

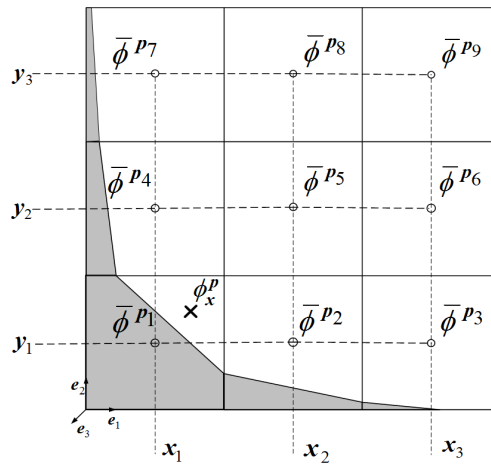


Figure 3.2: Stencil for the approximations of the parallel derivatives at the face centroid.

$$\bar{\phi}^{\mathbf{p}_1} = \frac{\phi_{(0,0,1)}^i + \phi_{(0,0,0)}^i}{2}, \bar{\phi}^{\mathbf{p}_2} = \frac{\phi_{(1,0,1)}^i + \phi_{(1,0,0)}^i}{2}, \bar{\phi}^{\mathbf{p}_3} = \frac{\phi_{(2,0,1)}^i + \phi_{(2,0,0)}^i}{2}, \quad (3.18)$$

$$\bar{\phi}^{\mathbf{p}_4} = \frac{\phi_{(0,1,1)}^i + \phi_{(0,1,0)}^i}{2}, \bar{\phi}^{\mathbf{p}_5} = \frac{\phi_{(1,1,1)}^i + \phi_{(1,1,0)}^i}{2}, \bar{\phi}^{\mathbf{p}_6} = \frac{\phi_{(2,1,1)}^i + \phi_{(2,1,0)}^i}{2}, \quad (3.19)$$

$$\bar{\phi}^{\mathbf{p}_7} = \frac{\phi_{(0,2,1)}^i + \phi_{(0,2,0)}^i}{2}, \bar{\phi}^{\mathbf{p}_8} = \frac{\phi_{(1,2,1)}^i + \phi_{(1,2,0)}^i}{2}, \bar{\phi}^{\mathbf{p}_9} = \frac{\phi_{(2,2,1)}^i + \phi_{(2,2,0)}^i}{2}. \quad (3.20)$$

By fitting the data $\bar{\phi}^{\mathbf{p}_k}$ ($k = 1 \dots 9$) with a biquadratic polynomial and calculating its x-directional derivatives at \mathbf{p} , we get

$$\phi_x^{\mathbf{p}} = \sum_{k=1}^9 \lambda_x^k \phi_x^{\mathbf{p}_k}, \quad (3.21)$$

with combination coefficients

$$\lambda_x^1 = \alpha_1 \beta_1, \lambda_x^2 = \alpha_2 \beta_1, \lambda_x^3 = \alpha_3 \beta_1, \quad (3.22)$$

$$\lambda_x^4 = \alpha_1 \beta_2, \lambda_x^5 = \alpha_2 \beta_2, \lambda_x^6 = \alpha_3 \beta_2, \quad (3.23)$$

$$\lambda_x^7 = \alpha_1 \beta_3, \lambda_x^8 = \alpha_2 \beta_3, \lambda_x^9 = \alpha_3 \beta_3, \quad (3.24)$$

where

$$\alpha_1 = \frac{(2x - x_2 - x_3)}{(x_1 - x_2)(x_1 - x_3)}, \alpha_2 = \frac{(2x - x_1 - x_3)}{(x_2 - x_1)(x_2 - x_3)}, \alpha_3 = \frac{(2x - x_1 - x_2)}{(x_3 - x_1)(x_3 - x_2)},$$

$$\beta_1 = \frac{(y - y_2)(y - y_3)}{(y_1 - y_2)(y_1 - y_3)}, \beta_2 = \frac{(y - y_1)(y - y_3)}{(y_2 - y_1)(y_2 - y_3)}, \beta_3 = \frac{(y - y_1)(y - y_2)}{(y_3 - y_1)(y_3 - y_2)}.$$

Similarly, we can construct interpolation $\phi_y^{\mathbf{p}}$. Both $\phi_x^{\mathbf{p}}$ and $\phi_y^{\mathbf{p}}$ are accurate to $O(h^2)$.

3.4 Boundary Conditions

In this section, we discuss the differentiation of the Dirichlet boundary condition (3.7). Our method is a generalization of the approach proposed by Schwartz et al. [94]. As shown in Fig 3.3 we choose a nine-cell stencil on each of the two planes P_1 and P_2 , both perpendicular to \mathbf{e}_s , where s is given by

$$\{s : |n_s^{\mathbf{B}}| \geq |n_k^{\mathbf{B}}|, k = 1, 2, 3\}. \quad (3.25)$$

In other words, \mathbf{e}_s is the axis-direction closest to the boundary normal $\mathbf{n}^{\mathbf{B}}$; \mathbf{x}_B is the centroid of the partial boundary included in the cell; \mathbf{p} and \mathbf{q} are the intersection points of \mathbf{e}_s with planes P_1 and P_2 , respectively. Then we define the distances from \mathbf{x}_B to the intersection points: $d_1 = \|\mathbf{x}_B - \mathbf{p}\|$ and $d_2 = \|\mathbf{x}_B - \mathbf{q}\|$.

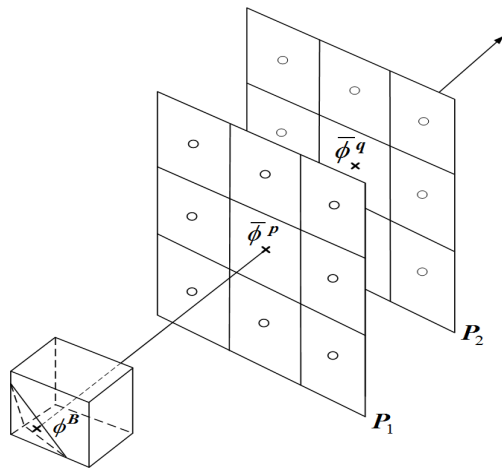


Figure 3.3: Stencil for the approximation of the derivatives at the boundary centroid.

As mentioned before, we need to approximate the gradient $\nabla\phi_B = (\phi_x^B, \phi_y^B, \phi_z^B)$ at the partial boundary centroid \mathbf{x}_B to $O(h^2)$ accuracy. To simplify the following discussion, we assume $\mathbf{e}_s = \mathbf{e}_1$. Then the approximation of ϕ_x^B is different from those of ϕ_y^B and ϕ_z^B . For the calculation of ϕ_x^B , we first use biquadratic interpolation to calculate $\bar{\phi}^{\mathbf{p}}$ and $\bar{\phi}^{\mathbf{q}}$, which are $O(h^3)$ accurate approximations to $\psi(\mathbf{p})$ and $\psi(\mathbf{q})$. The value of $\bar{\phi}^{\mathbf{p}}$ is a linear combination of the nine cell center values on plane P_1 , and $\bar{\phi}^{\mathbf{q}}$ is calculated analogously with values on P_2 . Then we combine the boundary value ϕ_x^B determined by the Dirichlet condition with the intersection values $\bar{\phi}^{\mathbf{p}}$ and $\bar{\phi}^{\mathbf{q}}$ using the scheme given in [94] to construct

$$\phi_x^B = \frac{1}{d_2 - d_1} \left(\frac{d_2}{d_1} (\phi_x^B - \bar{\phi}^{\mathbf{p}}) - \frac{d_1}{d_2} (\phi_x^B - \bar{\phi}^{\mathbf{q}}) \right). \quad (3.26)$$

To construct ϕ_y^B , we start by using the interpolation method in Eq. (3.21) to get $O(h^2)$ accurate approximations $\phi_y^{\mathbf{p}}$ and $\phi_y^{\mathbf{q}}$ with the nine cell center values on P_1 and P_2 , respectively. Then ϕ_y^B can be constructed by applying the following linear extrapolation to $\phi_y^{\mathbf{p}}$ and $\phi_y^{\mathbf{q}}$:

$$\phi_y^B = \frac{1}{d_2 - d_1} (d_2 \phi_y^{\mathbf{p}} - d_1 \phi_y^{\mathbf{q}}). \quad (3.27)$$

The same idea can be applied to the calculation of ϕ_z^B .

3.5 Calculation of Geometric Quantities Using Marching Tetrahedra Method

To approximate the basic geometric quantities κ_i , $\alpha_{i \pm \frac{1}{2} e_s}$, α_i^B , \mathbf{x}_i , $\mathbf{x}_{i \pm \frac{1}{2} e_s}$, \mathbf{x}_i^B , and \mathbf{n}_i^B with high accuracy, we employ the marching tetrahedra method, a widely used algorithm in computer graphics.

The underlying construction of the marching tetrahedra method is consistent with that of the embedded boundary method, in which the solution domains with complex geometries are embedded in a Cartesian grid. At the beginning stage, we calculate the signed distance of each node in the Cartesian grid to the embedded surface, which will be used in the following interpolations. In our case of cardiac simulations, the input data are 3D MRI photographs consisting of binary values for each pixel. A value of one means the position corresponding to that pixel locates inside the cardiac tissue, and a zero value means outside of the tissue [68]. Based on this binary values, the breadth-first search (BFS) algorithm [58] can be applied to calculate the signed distance to the embedded boundary for each Cartesian node.

Besides the requiring the signed distance to be available for each Cartesian nodes, the application of the marching tetrahedra algorithm also necessitate the division of each Cartesian cuboid into six tetrahedra. As shown in Fig. 3.4, each cuboid is cut in half three times. For each of the three pairs of opposite faces, we cut through them along a common diagonal direction. It is easy to see that all six resulting tetrahedra shares one of the main diagonals of the cuboid. As a result, we are also considering six face diagonals and one main diagonal, in addition to the twelve edges of the cuboid, a total of nineteen edges. Since we have the signed distances of both end points for each one of the nineteen edges, we can apply the linear interpolation technique to locate the

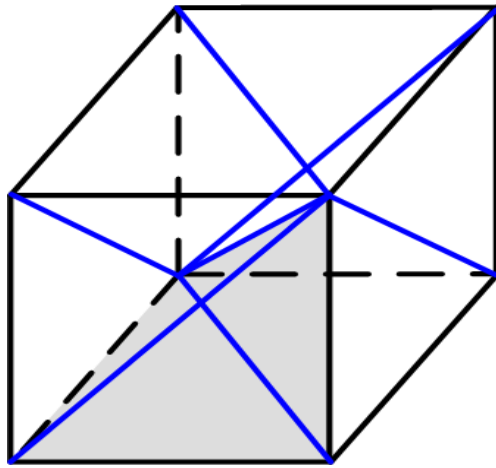


Figure 3.4: Divide each cube into six tetrahedra.

crossing point on each edge, which intersects with the embedded boundary.

For each of the six tetrahedra in a given cuboid, there are total 16 possible configurations, which falls into three distinct categories, i.e., no intersection; one vertex locates on a different side of the embedded boundary than the other three; two pairs of the four vertices locates on different sides of the boundary, as illustrated in Fig. 3.5. From this figure, it is easy to notice that the parts enclosed inside the embedded boundary are always tetrahedra or prisms, the centroids of faces and volume can be easily determined. With all these centroids, we can perform area or volume averaging over the six consisting tetrahedra to determine the aforementioned geometric quantities for all the cut cells.

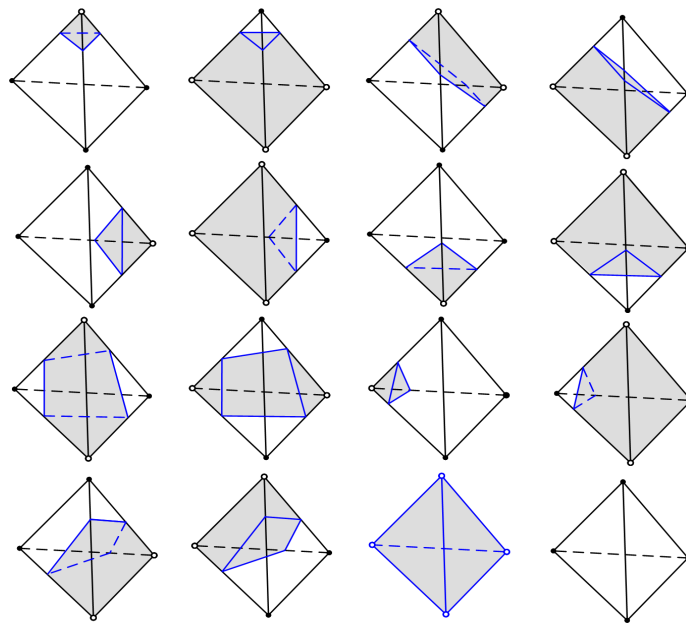


Figure 3.5: Different configurations of tetrahedra cut by the embedded interface.

Chapter 4

Verification

In this section, we verify the numerical algorithm with two tests. In the first test, we apply the EBM to solve the Poisson's equation with an anisotropic diffusion tensor in a 3D spherical domain. Second-order convergence is observed by comparing numerical to analytical solutions. In the second test, we solve the voltage equation with both EBM and PF in a slab geometry, where nearly identical transmembrane potentials and conduction velocities of the depolarizing wave front are observed in regions away from the boundaries. All the test results confirm the accuracy and correctness of the EBM.

4.1 Poisson's Equation in 3D Spherical Domain

Since the main challenge in solving the bidomain equations is the existence of elliptic operators with anisotropic diffusion tensors, we verify the new algorithm by solving an anisotropic Poisson equation. Within a spherical computational domain Ω

with center $(0, 0, 0)$ and radius 0.5, we solve the Poisson's equation with the Dirichlet boundary condition as:

$$\nabla \cdot (D\phi(\mathbf{x})) = f(\mathbf{x}) \quad \mathbf{x} \in \Omega, \quad (4.1)$$

$$\phi(\mathbf{x}) = \phi^B(\mathbf{x}) \quad \mathbf{x} \in \partial\Omega, \quad (4.2)$$

where the diffusion tensor D , the right-hand side function f , and the boundary value function ϕ^B are given as

$$D = \frac{1}{3} \begin{bmatrix} 7 & 2 & 1 \\ 2 & 6 & -2 \\ 1 & -2 & 5 \end{bmatrix}, \quad (4.3)$$

$$\begin{aligned} f(\mathbf{x}) = & -\frac{76}{3} \sin(x) \sin(2y) \sin(3z) - 8 \sin(x) \cos(2y) \cos(3z) \\ & + 2 \cos(x) \sin(2y) \cos(3z) + \frac{8}{3} \cos(x) \cos(2y) \sin(3z). \end{aligned} \quad (4.4)$$

$$\phi^B(\mathbf{x}) = \sin(x) \sin(2y) \sin(3z). \quad (4.5)$$

The analytical solution to the above boundary-value problem is

$$\phi^e(\mathbf{x}) = \sin(x) \sin(2y) \sin(3z). \quad (4.6)$$

It is worth noting that the choice of this analytical solution is solely for the purpose of convergence order analysis, and has no direct relation to the bidomain model. We use $\phi_{\mathbf{i}}$ and $\phi_{\mathbf{i}}^e$ to denote the numerical and corresponding exact solutions at the cell centroid $x_{\mathbf{i}}$, and define the L_1 , L_2 and L_∞ errors as:

$$\epsilon_1 = \sum_{\mathbf{i}} |\phi_{\mathbf{i}} - \phi_{\mathbf{i}}^e| h^3 \kappa_{\mathbf{i}}, \quad (4.7)$$

$$\epsilon_2 = \left(\sum_{\mathbf{i}} |\phi_{\mathbf{i}} - \phi_{\mathbf{i}}^e|^2 h^3 \kappa_{\mathbf{i}} \right)^{\frac{1}{2}}, \quad (4.8)$$

$$\epsilon_\infty = \max_{\mathbf{i}} |\phi_{\mathbf{i}} - \phi_{\mathbf{i}}^e|, \quad (4.9)$$

where h is the space step size and $\kappa_{\mathbf{i}}$ is the volume fraction. To estimate the order of convergence, we consider mesh sizes of 16, 32, 64, and 128, denoted by grids I, II, III, and IV, respectively. In Table 4.1, we show the orders of convergence deduced from the three types of errors under different mesh sizes. The entries from the last three columns of Table 4.1 confirm the second-order accuracy of the method.

4.2 Comparison of EBM and PF

We compare EBM and PF for the solution of the voltage equation in a slab geometry. The transmembrane potential (V) and the conduction velocity (CV) of the

Table 4.1: Orders of convergence for three types of errors

Error Type	I	II	III	IV	I / II	II / III	III / IV
ϵ_1	6.13e-4	7.04e-5	1.47e-5	3.59e-6	3.12	2.26	2.03
ϵ_2	1.03e-3	9.52e-5	1.86e-5	4.64e-6	3.44	2.36	2.00
ϵ_∞	1.18e-2	1.20e-3	1.39e-4	1.87e-5	3.29	3.12	2.89

depolarizing wave front are compared in the center of the slab, away from its boundaries. By this measure, the two methods are nearly identical. The reason for this near identity is that the compared statistics are not influenced by boundary effects, while it is only in the boundary effects that the methods differ.

We choose the slab region $[0, 1.0] \times [0, 0.5] \times [0, 2.0]$ (cm). The direction of cardiac fibers is chosen to be parallel to the z-axis. An initial stimulus is applied in a region at the bottom of the slab.

Five mesh sizes are considered, starting from $\Delta x = 1.0$ mm, with each following mesh refined by a factor of 2. The starting Δx is quite coarse compared to the typical size of cardiac cells, which is approximately $100 \mu\text{m}$ long and $10\text{-}25 \mu\text{m}$ in diameter [97]. The finest mesh is used to calculate errors in the other four cases. The difference for this fiducial grid is smaller than the mesh differences, indicating that the two codes are converging to a common solution.

Table. 4.2 shows the errors and order of convergence for *CV*. In Table. 4.3 we present the error analysis and convergence orders based on comparison of L_1 norms of V . It is shown that both PF and EBM methods converge in first order. To achieve second order accuracy in both time and space, second-order operator-splitting schemes, e.g., Strang splitting [98], need to be applied to the bidomain equations.

Table 4.2: CV error and convergence order comparison

Mesh Size	PF Err	PF Order	EBB Err	EBM Order	PF – EBM
$15 \times 10 \times 25$	3.43e-02		3.51e-02		7.77e-02
$30 \times 20 \times 50$	1.89e-02	0.86	1.72e-02	1.03	1.71e-03
$60 \times 40 \times 100$	0.742e-02	1.35	0.612e-02	1.49	1.29e-03
$120 \times 80 \times 200$	0.151e-02	2.30	0.147e-02	2.06	3.14e-05
$240 \times 160 \times 400$					1.46e-06

Table 4.3: $V(L_1\text{-norm})$ error and convergence order comparison

Mesh Size	PF Err	PF Order	EBM Err	EBM Order	PF – EBM
$15 \times 10 \times 25$	5.19e-01		5.30e-01		7.44e-02
$30 \times 20 \times 50$	2.06e-01	1.34	1.86e-01	1.51	2.11e-02
$60 \times 40 \times 100$	0.729e-01	1.50	0.689e-01	1.43	4.09e-03
$120 \times 80 \times 200$	0.178e-01	2.03	0.174e-01	1.99	5.11e-04
$240 \times 160 \times 400$					1.08e-04

Chapter 5

Applications

The main motivation of this work is to develop an improved numerical method to support the study of the low-energy antifibrillation pacing (LEAP) initiative [70], whose effect depends on the successful generation of virtual electrodes in the vicinities of heterogeneities in the myocardium. As a result, the accurate resolution of small features, e.g., blood vessels, plays an essential role in defibrillation simulations. In this section, we first demonstrate the strength of our EBM method by showing the voltage distribution on blood vessel walls during a defibrillation event. The calculation is representative of ones needed to determine the smallest relevant blood vessels for consideration. With the blood vessel size fixed, a systematic statistical analysis gives suggestions on the choice of appropriate mesh resolutions for practical defibrillation simulations on complex 3D domains. Because optimization, V&V and UQ typically require a large number of simulations, determination of minimum mesh requirements is important.

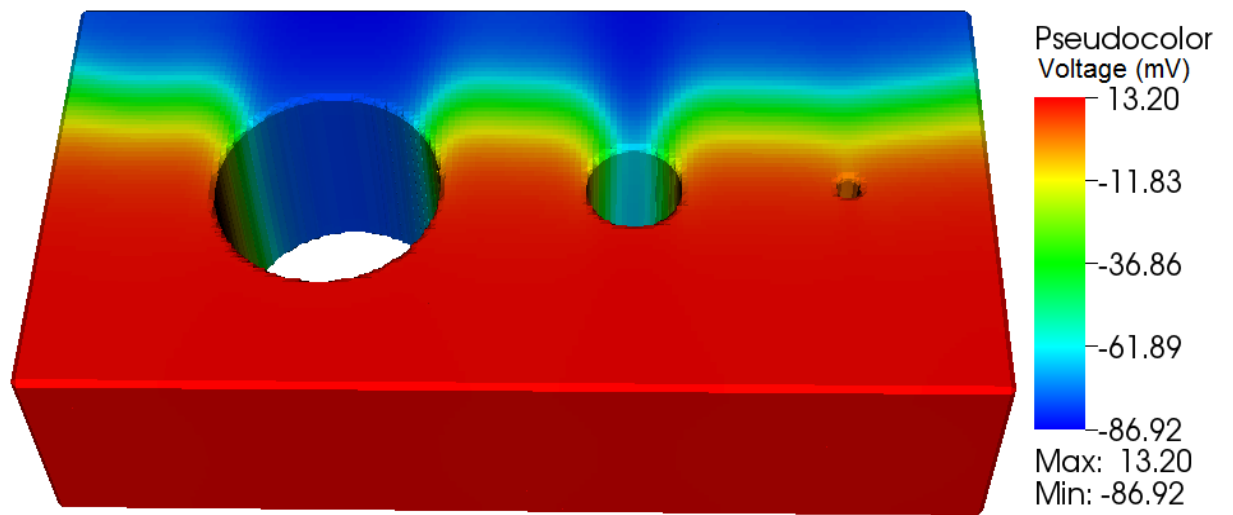


Figure 5.1: Transmembrane potential (mV) in a slab before applying the defibrillation shock.

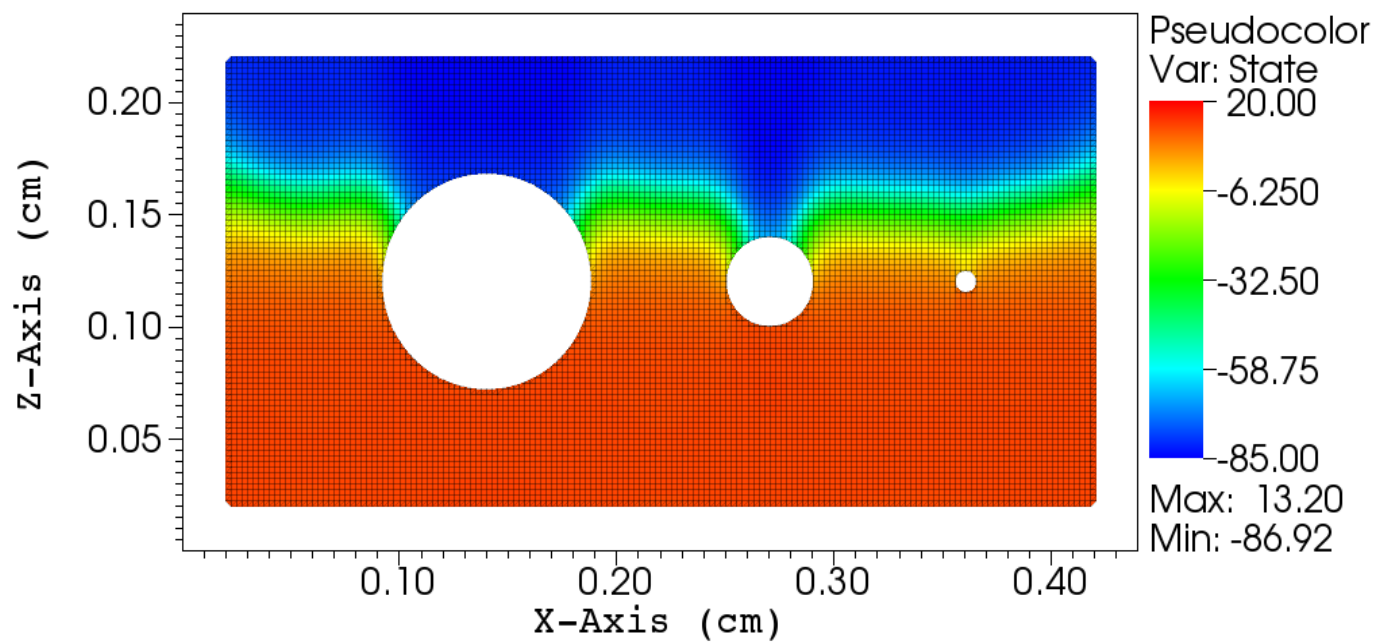


Figure 5.2: Cross section view of the transmembrane potential before applying the defibrillation shock.

5.1 Defibrillation Simulation

Defibrillation consists of one or more strong voltage pulses applied across the heart. This voltage is originally applied to the extracellular space, and so the coupling of this signal to the intracellular voltages is essential for defibrillation to succeed. The dual voltage systems and the coupling between them is described by the bidomain model as discussed in Chap. 5.

Our simulation domain is chosen to be a slab taken from a segment of the heart wall, with dimensions $[0, 4] \times [0, 1] \times [0, 2]$ (mm). The spatial resolution is 0.025 (mm) and the time step size is 0.01 (ms). The values of conductivities of the cardiac tissue \mathbb{H} and the surrounding tissue \mathbb{T} are chosen as in [24]. Three blood vessels are placed perpendicular to the xz -plane, with radii ranging from 50 to 500 microns, which are typical sizes found in coronary vasculature [70, 8]. It should be emphasized that although the two larger vessels, 40 and 16 mesh cells in diameter, respectively, can be resolved in both PF and EBM methods, the smallest one with only 4 mesh cells in diameter can not be captured correctly in the PF model, due to its artificial transition layers.

As shown in Fig. 5.1, an initial stimulus is applied to the bottom of the slab, resulting a depolarization wave-front propagating upwards. To assist the observation of potential distributions in the vicinity of blood vessels, in Fig. 5.2 we show the 2D cross section view of the same simulation as in Fig. 5.1. When the wave-front passes the blood vessels, a defibrillation shock of strength 5 V/cm in the x -direction is applied to the slab. Shortly after the defibrillation shock, as illustrated in Fig. 5.3, voltage drops are observed across all three blood vessels. In fact, the electrical discontinuity introduced by the blood vessels acts as a source for the transfer of the shock energy from

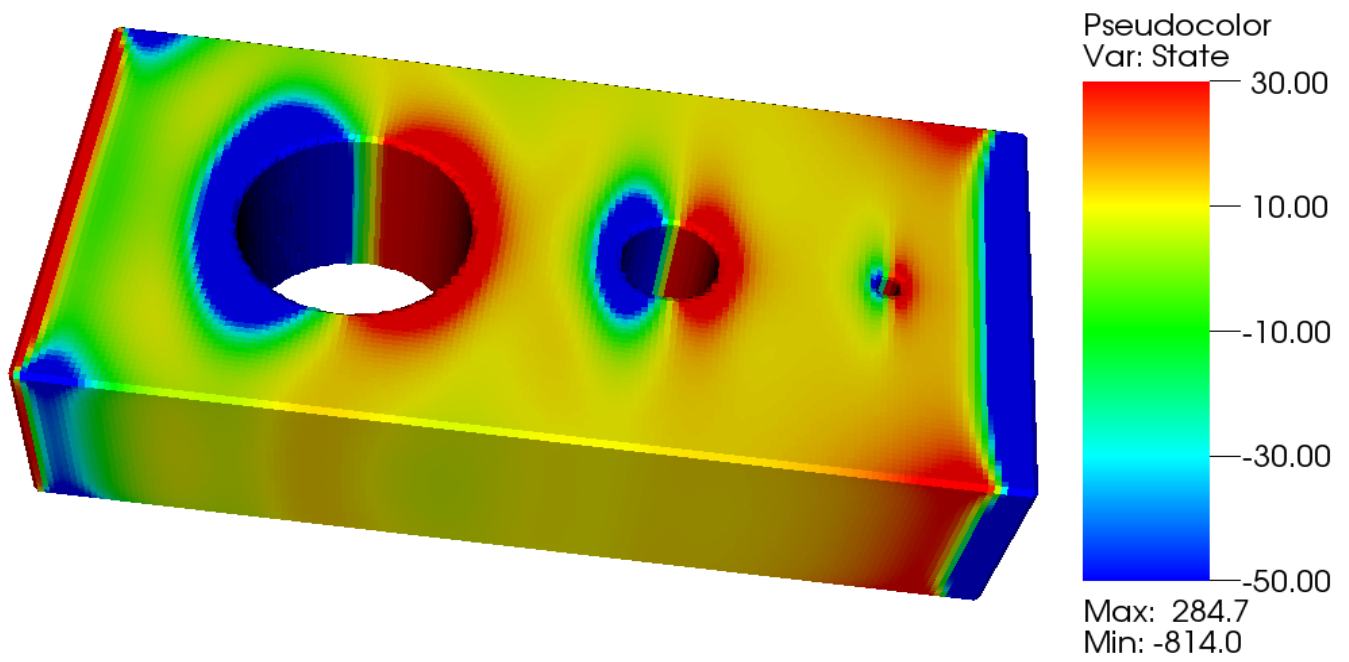


Figure 5.3: Transmembrane potential (mV) in a slab after applying the defibrillation shock.

the intracellular domain to the cardiac cell domain, which expedites the defibrillation process.

5.2 Mesh Resolution

The determination of a proper mesh resolution is a prerequisite for any defibrillation simulation. To make suggestions for the choice of appropriate mesh resolutions for practical simulations on complex domains, a systematic statistical analysis is performed using a simplified slab geometry as that in Sec 5.1. We consider a slab region $[-0.2, 0.2] \times [-0.2, 0.2] \times [-0.2, 0.2]$ (mm), in which a blood vessel with diameter 0.1 mm is located perpendicular to the xz -plane. The cardiac cells in the slab are initialized by the resting membrane potential, then a shock of strength 5V/cm in the x -direction is applied for 0.1 ms.

To perform a statistical analysis of the effect of the mesh resolution on wave propagation across the blood vessel, we perform multiple simulations with different combinations of mesh resolutions and positions of the blood vessel. Eight resolution levels are adopted, with the diameter of the blood vessel ranging from $2\Delta x$ to $8\Delta x$ in mesh units. For each mesh resolution, we choose one of 25 positions within the small region $[-\Delta x, \Delta x] \times [-\Delta x, \Delta x]$ as the crossing point of the blood vessel axis and the xz -plane. The voltage drops across the blood vessel are calculated for different combinations, and the results are summarized in Fig. 5.4.

In Fig. 5.4, the bottom and top of the box are the first quartile (Q_1) and third quartile (Q_3), respectively. The band inside the box denotes the median. The lower and upper ends of the whisker are the minimum and maximum of the data. From the

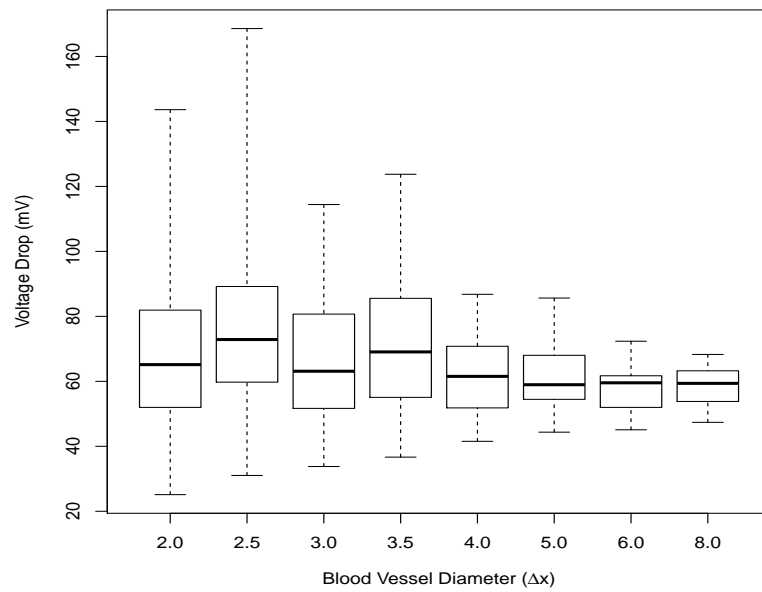


Figure 5.4: Variation of the voltage drop across the blood vessel under mesh refinement.

plot, we can observe a fast convergence of the voltage drop as the resolution increases. With only a $4\Delta x$ diameter, the relative error in the voltage drop calculation is already within 10%, when taking the $8\Delta x$ values as accurate. Moreover, even in the case of a resolution as low as $2\Delta x$, the calculated voltage drops are still within a reasonably small neighborhood of the $8\Delta x$ resolution results. In conclusion, four or fewer cells across the blood vessel should suffice in a whole heart simulation for the purpose of UQ analysis, while higher resolutions are necessary for fully accurate whole heart simulations. Further efforts to improve the algorithm could reduce these numbers.

Chapter 6

Conclusions

We extend the finite volume embedded boundary method (EBM), originally proposed by Johansen and Colella [50], to the solutions of elliptic and parabolic equations involving anisotropic diffusion tensors and indicate a methodology for construction of solutions of an arbitrary order of accuracy. A new type of sharp-boundary electrocardiac simulation tool based on the EBM method is introduced and applied to defibrillation studies using the bidomain model. It is shown that the new method is second-order-accurate uniformly up to boundaries, which particularly aids the resolution of small features in the heart tissue. This capability lends our method to the promising field of low-energy defibrillation, where the generation of virtual electrodes around small heterogeneities in the myocardium plays an indispensable role. To improve the efficiency as well as to keep the accuracy of practical simulations, a systematic statistical analysis is performed in order to determine the appropriate mesh resolution. It is shown that four mesh cells are needed to resolve the finest blood vessels for the purpose of UQ analysis. However, for highly accurate whole heart simulations, the usage of more mesh cells is recommended. To further improve the accuracy, in

the future, we plan to add more physiological details, such as the 3D complex heart geometry, realistic myocardial fiber orientations, and more complete models of ionic currents, into our model. Extensions to higher-order accuracy may be beneficial to further reduce resolution requirements. Second order accuracy in time (not considered here) will require Strang splitting of the sequential equation solution method.

Bibliography

- [1] R. J. Adams and et al. Heart disease and stroke statistics-2010 update: A report from the american heart association. *Circulation*, 121:46–215, 2009.
- [2] Michael J. Aftosmis, Marsha J. Berger, and John E. Melton. Robust and efficient cartesian mesh generation for component-based geometry. *AIAA journal*, 36(6):952–960, 1998.
- [3] Rubin R. Aliev and Alexander V. Panfilov. A simple two-variable model of cardiac excitation. *Chaos, Solitons and Fractals*, 7(3):293–301, 1996.
- [4] Travis M. Austin, Mark L. Trew, and Andrew J. Pullan. Solving the cardiac bidomain equations for discontinuous conductivities. *IEEE Transactions on Biomedical Engineering*, 53(7):1265–1272, 2006.
- [5] C. Beckermann, H. J. Diepers, I. Steinbach, A. Karma, and X. Tong. Modeling melt convection in phase-field simulations of solidification. *Journal of Computational Physics*, 154(2):468–496, 1999.
- [6] Richard P Beyer. A computational model of the cochlea using the immersed boundary method. *Journal of Computational Physics*, 98(1):145–162, 1992.
- [7] M. Bishop and G. Plank. Representing cardiac bidomain bath-loading effects by

an augmented monodomain approach: application to complex ventricular models. *Biomedical Engineering*, 58(4):1066–1075, 2011.

- [8] M. Bishop, G. Plank, and E. Vigmond. Investigating the role of coronary vascluture in the mechanisms of defibrillation. *Circulation: Arrhythmia and Electrophysiology*, pages 210–219, 2012. See also supplementary material.
- [9] G. Bub, A. Shrier, and L. Glass. Spiral wave generation in heterogenous excitable media. *Physical Review Letters*, 88:101–114, 2002.
- [10] G. Buzzard, J. Fox, and F. Siso-Nadal. Sharp interface and voltage conservation in the phase field method: Application to cardiac electrophysiology. *SIAM Journal on Scientific Computing*, 34(2):837–854, 2008.
- [11] Juan R. Cebral and R. Lohner. Efficient simulation of blood flow past complex endovascular devices using an adaptive embedding technique. *Medical Imaging*, 24(4):468–476, 2005.
- [12] M. Chebbok and et al. Low-energy anti-fibrillation pacing (leap): a gentle, non traumatic defibrillation option. *European Heart Journal*, 33:381, 2012.
- [13] Elizabeth M. Cherry and Flavio H. Fenton. A tale of two dogs: analyzing two models of canine ventricular electrophysiology. *American Journal of Physiology-Heart and Circulatory Physiology*, 292:43–55, 2007.
- [14] Elizabeth M. Cherry, Flavio H. Fenton, and Robert F. Gilmour. Mechanisms of ventricular arrhythmias: a dynamical systems-based perspective. *American Journal of Physiology-Heart and Circulatory Physiology*, 302:2451–2463, 2012.
- [15] T. J. Chung. Finite element analysis in fluid dynamics. Report No. STI/Recon Technical Report: 44102, NASA, 1978.

- [16] R. Clayton and et al. Models of cardiac tissue electrophysiology: Progress, challenges and open questions. *Progress in Biophysics and Molecular Biology*, 104:22–48, 2011.
- [17] R. Clayton and A. Panfilov. A guide to modelling cardiac electrical activity in anatomically detailed ventricles. *Progress in Biophysics and Molecular Biology*, 96:19–43, 2008.
- [18] P. Colella, M. Dorr, J. Hittinger, D. Martin, and P. McCorquodale. High-order finite-volume adaptive methods on locally rectangular grids. *Journal of Physics: Conference Series*, 180:1, 2009.
- [19] R. K. Crockett, P. Colella, and D. T. Graves. A cartesian grid embedded boundary method for solving the poisson and heat equations with discontinuous coefficients in three dimensions. *Journal of Computational Physics*, 230(7):2451–2469, 2010.
- [20] A. Dadone and B. Grossman. Ghost-cell method for inviscid two-dimensional flows on cartesian grids. *AIAA Journal*, 42(12):2499–2507, 2004.
- [21] A. Dadone and B. Grossman. Ghost-cell method for analysis of inviscid three-dimensional flows on cartesian-grids. *Computers & fluids*, 36(10):1513–1528, 2007.
- [22] Gouri Dhatt, Emmanuel Lefrançois, and Gilbert Touzot. *Finite element method*. John Wiley & Sons, 2012.
- [23] Robert Dillon, Lisa Fauci, Aaron Fogelson, and Donald Gaver III. Modeling biofilm processes using the immersed boundary method. *Journal of Computational Physics*, 129(1):57–73, 1996.

- [24] R. W. Dos Santos, G. Plank, S. Bauer, and E. J Vigmond. Preconditioning techniques for the bidomain equations. *Domain Decomposition Methods in Science and Engineering*, pages 571–580, 2005.
- [25] G. Duckett and D. Barkley. Modeling the dynamics of cardiac action potential. *Phys. Rev. Lett.*, 85:884, 2000.
- [26] P. A. Durbin and G. Iaccarino. An approach to local refinement of structured grids. *Journal of Computational Physics*, 181(2):639–653, 2002.
- [27] D. Durrer, R.T. van Dam, G.E. Freud, M.J. Janse, F.L. Meijler, and R.C Arzbaeher. Total excitation of the isolated human heart. *Circulation*, 41:899–912, 1970.
- [28] I.R. Efimov, V.P. Nikolski, and G. Salama. Optical imaging of the heart. *Circulation Research*, 286:2183–2194, 2004.
- [29] V.G. Fast and A.G. Kleber. Macroscopic conduction in cultured strands of neonatal rat heart cells measured with voltage-sensitive dyes. *Circulation Research*, 73:914–925, 1993.
- [30] F. Fenton and E. Cherry. Models of cardiac cell. *Chaos*, 8(1):20–47, 1998.
- [31] F. Fenton, E. Cherry, A. Karma, and W.Rappel. Modeling wave propagation in realistic heart geometries using the phase-field method. *Chaos*, 15(1):013502, 2005.
- [32] F. Fenton and A. Karma. Vortex dynamics in three-dimensional continuous myocardium with fiber rotation: Filament instability and fibrillation. *Chaos*, 8(1):20–47, 1998.

- [33] Flavio H. Fenton, Alessio Gizzi, Christian Cherubini, Nicola Pomella, and Simonetta Filippi. Role of temperature on nonlinear cardiac dynamics. *Physical Review E*, 87(4):042717, 2013.
- [34] Flavio H. Fenton, Stefan Luther, Elizabeth M. Cherry, Niels F. Otani, Valentin Krinsky, Alain Pumir, Eberhard Bodenschatz, and Robert F. Gilmour. Termination of atrial fibrillation using pulsed low-energy far-field stimulation. *Circulation*, 120(6):467–476, 2009.
- [35] Simonetta Filippi, Alessio Gizzi, Christian Cherubini, Stefan Luther, and Flavio H. Fenton. Mechanistic insights into hypothermic ventricular fibrillation: The role of temperature and tissue size. *Europace*, 16(3):424–434, 2014.
- [36] Richard FitzHugh. Impulses and physiological states in theoretical models of nerve membrane. *Biophysical Journal*, 1(6):445, 1961.
- [37] Leopoldo P. Franca, Sergio L. Frey, and Thomas JR Hughes. Stabilized finite element methods: I. application to the advective-diffusive model. *Computer Methods in Applied Mechanics and Engineering*, 95(2):253–276, 1992.
- [38] P. C. Franzone, L. F. Pavarino, and B. Taccardi. Simulating patterns of excitation, repolarization and action potential duration with cardiac bidomain and monodomain models. *Mathematical Biosciences*, 197(1):35–66, 2005.
- [39] Kikuchi Fumio. Mixed and penalty formulations for finite element analysis of an eigenvalue problem in electromagnetism. *Computer Methods in Applied Mechanics and Engineering*, 64(1):509–521, 1987.
- [40] Frederic Gibou, Ronald Fedkiw, Li-Tien Cheng, and Myungjoo Kang. A second-

- order-accurate symmetric discretization of the poisson equation on irregular domains. *Journal of Computational Physics*, 176(1):205–227, 2002.
- [41] J. Glimm, J. W. Grove, X.-L. Li, and N. Zhao. Simple front tracking. In G.-Q. Chen and E. DiBenedetto, editors, *Contemporary Mathematics*, volume 238, pages 133–149. Amer. Math. Soc., Providence, RI, 1999.
- [42] J. Glimm, X.-L. Li, Y.-J. Liu, and N. Zhao. Conservative front tracking and level set algorithms. *Proc. National Academy of Sci.*, 98:14198–14201, 2001.
- [43] R.A. Gray, A.M. Pertsov, and J. Jalife. Spatial and temporal organization during cardiac fibrillation. *Nature*, 392:75–78, 1998.
- [44] Anita Hansbo and Peter Hansbo. A finite element method for the simulation of strong and weak discontinuities in solid mechanics. *Computer methods in applied mechanics and engineering*, 193(33):3523–35404, 2004.
- [45] David M. Harrild, R. Christian Penland, and Craig S. Henriquez. A flexible method for simulating cardiac conduction in three-dimensional complex geometries. *Journal of Electrocardiology*, 33(3):241–251, 2000.
- [46] Elvio A. Heidenreich, Jose M. Ferrero, Manuel Doblare, and Jose F. Rodriguez. Adaptive macro finite elements for the numerical solution of monodomain equations in cardiac electrophysiology. *Annals of Biomedical Engineering*, 38(7):2331–2345, 2010.
- [47] Craig S Henriquez. Simulating the electrical behavior of cardiac tissue using the bidomain model. *Critical reviews in biomedical engineering*, 21:1–77, 1992.
- [48] Thomas JR Hughes, L. P. Franca, and M. Mallet. A new finite element formulation for computational fluid dynamics: I. symmetric forms of the compressible

- euler and navier-stokes equations and the second law of thermodynamics. *Computer Methods in Applied Mechanics and Engineering*, 54(2):223–234, 1986.
- [49] V. Iyer and et al. A computational model of the human left-ventricular epicardial myocyte. *Biophysical Journal*, 87(3):1507–1525, 2004.
- [50] H. Johansen and P. Colella. A Cartesian grid embedded boundary method for Poisson’s equation on irregular domains. *J. Comput. Phys*, 147:60–85, 1998.
- [51] Peter R. Johnston. A finite volume method solution for the bidomain equations and their application to modelling cardiac ischaemia. *Computer Methods in Biomechanics and Biomedical Engineering*, 13(2):157–170, 2010.
- [52] Eunok Jung and Charles S. Peskin. Two-dimensional simulations of valveless pumping using the immersed boundary method. *SIAM Journal on Scientific Computing*, 23(1):19–45, 2001.
- [53] Kunihiko Kaneko. Overview of coupled map lattices. *Chaos: An Interdisciplinary Journal of Nonlinear Science*, 2:279–282, 1992.
- [54] A. Karma and W. J. Rappel. Phase-field method for computationally efficient modeling of solidification with arbitrary interface kinetics. *Physical Review E*, 53(4):3017, 1996.
- [55] J. P. Keener and K. Bogar. A numerical method for the solution of the bidomain equations in cardiac tissue. *Chaos: An Interdisciplinary Journal of Nonlinear Science*, 8(1):234–241, 1998.
- [56] Tusscher KH and Panfilov AV. Modelling of the ventricular conduction system. *Prog Biophys Mol Biol*, 96:152–170, 2008.

- [57] A.G. Kleber and Y. Rudy. Basic mechanisms of cardiac impulse propagation and associated arrhythmias. *Physiological Reviews*, 84:431–488, 2004.
- [58] Donald Ervin Knuth. *The art of computer programming: sorting and searching*. Pearson Education, New York, 1998.
- [59] Julien Kockelkoren, Herbert Levine, and Wouter-Jan Rappel. Computational approach for modeling intra-and extracellular dynamics. *Physical Review E*, 68(3):37702, 2003.
- [60] Dimitris C. Lagoudas, Zhonghe Bo, and Muhammad A. Qidwai. A unified thermodynamic constitutive model for sma and finite element analysis of active metal matrix composites. *Mechanics of Composite Materials and Structures*, 3(2):153–179, 1996.
- [61] Long Lee and R. J. LeVeque. An immersed interface method for incompressible Navier-Stokes equations. *SIAM J. Sci. Comput.*, 25:832–856, 2003.
- [62] S. S. Lee and R. A. Westmann. Application of high-order quadrature rules to time-domain boundary element analysis of viscoelasticity. *International Journal for Numerical Methods in Engineering*, 38:607–629, 1995.
- [63] R. J. LeVeque. Immersed interface methods for Stokes flow with elastic boundaries or surface tension. *SIAM J. Sci. Comput.*, 18:709–735, 1997.
- [64] R. J. LeVeque and Z.-L. Li. The immersed interface method for elliptic equations with discontinuous coefficients and singular sources. *SIAM J. Num. Anal.*, 31:1019–1044, 1994.
- [65] Zhilin Li. An overview of the immersed interface method and its applications. *Taiwanese J. Mathematics*, 7:1–49, 2003.

- [66] Rainald Lohner and Joseph D. Baum. Adaptive h-refinement on 3d unstructured grids for transient problems. *International Journal for Numerical Methods in Fluids*, 14(12):1407–1419, 1992.
- [67] W. E. Lorensen and H. E. Cline. Marching cubes: A high resolution 3D surface construction algorithm. *Computer Graphics*, 21(4):163–169, 1987.
- [68] Maria Lorenzo-Valdes, Gerardo I. Sanchez-Ortiz, Raad Mohiaddin, and Daniel Rueckert. Atlas-based segmentation and tracking of 3d cardiac mr images using non-rigid registration. *Medical Image Computing and Computer-Assisted Intervention*, 1:642–650, 2002.
- [69] Haoxiang Luo, Rajat Mittal, Xudong Zheng, Steven A. Biela, Raymond J. Walsh, and James K. Hahn. An immersed boundary method for flow structure interaction in biological systems with application to phonation. *Journal of Computational Physics*, 227(22):9303–9332, 2008.
- [70] Stefan Luther, Flavio H. Fenton, Bruce G. Kornreich, Amgad Squires, Philip Bittihn, Daniel Hornung, and Markus Zabel et al. Low-energy control of electrical turbulence in the heart. *Nature*, 475(7355):235–239, 2011.
- [71] P. McCorquodale, P. Colella, and H. Johansen. A Cartesian grid embedded boundary method for the heat equation on irregular domains. *J. Comput. Phys.*, 273:620–635, 2001.
- [72] Z. H. Ming, Y. L. Soo, S. Huang, Y. H. Kao, J. C. Tsang, and S. S. Iyer. Three dimensions elasto-plastic finite element analysis for the surrounding rock stability of large-scale underground openings. *Chinese Journal of Rock Mechanics and Engineering*, 1:5, 1987.

- [73] R. Mittal and G. Iaccarino. Immersed boundary methods. *Annu. Rev. Fluid Mech.*, 37:239–261, 2005.
- [74] Keith L. Moore, Arthur F. Dalley, and Anne M. R. Agur. *Clinically Oriented Anatomy*. Lippincott Williams and Wilkins, 2013.
- [75] Chamakuri Nagaiah and Karl Kunisch. Higher order optimization and adaptive numerical solution for optimal control of monodomain equations in cardiac electrophysiology. *Applied Numerical Mathematics*, 61(1):53–65, 2011.
- [76] Kai Nagel and Michael Schreckenberg. A cellular automaton model for freeway traffic. *Journal de physique*, 2:2221–2229, 1992.
- [77] J.C. Neu and W. Krassowska. Homogenization of syncytial tissues. *Critical Reviews in Biomedical Engineering*, 21:137–199, 1993.
- [78] S. J. Osher and R. P. Fedkiw. *Level Sets and Dynamic Implicit Surfaces*. Springer-Verlag, New York, 2002. ISBN 0387954821.
- [79] Alexandre Panfilov and Pauline Hogeweg. Spiral breakup in a modified fitzhugh-nagumo model. *Physics Letters A*, 176(5):295–299, 1993.
- [80] N. A. Patankar. A formulation for fast computations of rigid particulate flows. *Center for Turbulence Research Annual Research Briefs*, pages 185–196, 2001.
- [81] P. Pathmanathan, M. S. Shotwell, D. J. Gavaghan, J. M. Cordeiro, and R. A. Gray. Uncertainty quantification of fast sodium current steady-state inactivation for multi-scale models of cardiac electrophysiology. *Prog. Biophys. Mol. Biol.*, 117(1):4–18, 2015.

- [82] Macklin Paul and John S. Lowengrub. A new ghost cell-level set method for moving boundary problems: application to tumor growth. *Journal of scientific computing*, 35(2-3):266–299, 2008.
- [83] R. Christian Penland, David M. Harrild, and Craig S. Henriquez. Modeling impulse propagation and extracellular potential distributions in anisotropic cardiac tissue using a finite volume element discretization. *Computing and Visualization in Science*, 4(4):215–226, 2002.
- [84] Oliver Penrose and Paul C. Fife. Thermodynamically consistent models of phase-field type for the kinetic of phase transitions. *Physica D: Nonlinear Phenomena*, 43(1):44–62, 1990.
- [85] C. S. Peskin. Flow patterns around heart valves: a numerical method. *J. Comput. Phys.*, 10:252–271, 1972.
- [86] C. S. Peskin. Numerical analysis of blood-flow in heart. *J. Comput. Phys.*, 25:220–252, 1977.
- [87] C. S. Peskin. The immersed boundary method. *Acta Numer.*, 11:479–517, 2002.
- [88] Brendan Phibbs. *The human heart: a basic guide to heart disease*. Lippincott Williams & Wilkins, Philadelphia, PA, 2007.
- [89] Jan Pomplun, Sven Burger, Lin Zschiedrich, and Frank Schmidt. Adaptive finite element method for simulation of optical nano structures. *Physica status solidi*, 244(10):3419–3434, 2007.
- [90] Mark Potse, Bruno Dube, Jacques Richer, Alain Vinet, and Ramesh M. Gulrajani. A comparison of monodomain and bidomain reaction-diffusion models

- for action potential propagation in the human heart. *IEEE Transactions on Biomedical Engineering*, 53(12):2425–2435, 2006.
- [91] Jack M. Rogers and Andrew D. McCulloch. A collocation-galerkin finite element model of cardiac action potential propagation. *IEEE Transactions on Biomedical Engineering*, 41(8):743–757, 1994.
- [92] Nizar Ben Salah, Azzeddine Soulaïmani, and Wagdi G. Habashi. A finite element method for magnetohydrodynamics. *Computer methods in applied mechanics and engineering*, 190(43):5867–5892, 2001.
- [93] R. Samulyak, J. Du, J. Glimm, and Z. Xu. A numerical algorithm for MHD of free surface flows at low magnetic Reynolds numbers. *J. Comput. Phys.*, 226:1532–1546, 2007.
- [94] P. Schwartz, M. Barad, P. Colella, and T. Ligocki. A Cartesian grid embedded boundary method for the heat equation and Poisson’s equation in three dimensions. *J. Comput. Phys.*, 211:531–550, 2006.
- [95] Sarah B. Scruggs and R. John Solaro. The significance of regulatory light chain phosphorylation in cardiac physiology. *Archives of biochemistry and biophysics*, 510(2):129–134, 2011.
- [96] Nestor G. Sepulveda, Bradley J. Roth, and J. P. Wikswo. Current injection into a two-dimensional anisotropic bidomain. *Biophysical Journal*, 55:987–999, 1989.
- [97] Daniel Sevcovic. The cardiac muscle cell. *Bioessays*, 22(2):188–199, 2000.
- [98] G. Strang. On the construction and comparison of difference schemes. *SIAM J. Numer. Anal.*, 5(3):506–517, 1968.

- [99] G. Strang and G. Fix. *An Analysis of the Finite Element Method*. Prentice-Hall, Englewood Cliffs, 1973.
- [100] Lei Tang and James D. Baeder. Uniformly accurate finite difference schemes for p-refinement. *SIAM Journal on Scientific Computing*, 20(3):1115–1131, 1998.
- [101] Graham M. Treece, Richard W. Prager, and Andrew H. Gee. Regularised marching tetrahedra: improved iso-surface extraction. *Computers & Graphics*, 23(4):583–598, 1999.
- [102] Mark Trew, Ian Le Grice, Bruce Smaill, and Andrew Pullan. A finite volume method for modeling discontinuous electrical activation in cardiac tissue. *Annals of Biomedical Engineering*, 33(5):590–602, 2005.
- [103] Yu-Heng Tseng and Joel H. Ferziger. A ghost-cell immersed boundary method for flow in complex geometry. *Journal of Computational Physics*, 192(2):593–623, 2003.
- [104] Ten Tusscher, Kirsten HWJ, Olivier Bernus, and Alexander V. Panfilov. Comparison of electrophysiological models for human ventricular cells and tissues. *Prog Biophys Mol Biol*, 90(1):326–345, 2006.
- [105] H. S. Udaykuma, W. Shyy, and M. M. Rao. A mixed eulerian lagrangian method for fluid flows with complex and moving boundaries. *International journal for numerical methods in fluids*, 22(8):691–712, 1996.
- [106] Kevin Wang, Arthur Rallu, J. F. Gerbeau, and Charbel Farhat. Algorithms for interface treatment and load computation in embedded boundary methods for fluid and fluid structure interaction problems. *International Journal for Numerical Methods in Fluids*, 67(9):1175–1206, 2011.

- [107] S. Wang, J. Glimm, R. Samulyak, X. Jiao, and C. Diao. An embedded boundary method for two phase incompressible flow. 2013. arXiv:1304.5514.
- [108] Shuqiang Wang, Roman V Samulyak, and Tongfei Guo. An embedded boundary method for elliptic and parabolic problems with interfaces and application to multi-material systems with phase transitions. *Acta Mathematica Scientia*, 30B(2):499–521, 2010.
- [109] MA Watanabe, FH Fenton, SJ Evans, HM Hastings, and A Karma. Mechanisms for discordant alternans. *Computers & Fluids*, 12(2):196–206, 2001.
- [110] James B. White, Gregory P. Walcott, Andrew E. Pollard, and Raymond E. Ideker. Myocardial discontinuities: a substrate for producing virtual electrodes that directly excite the myocardium by shocks. *Circulation*, 97(17):1738–1745, 1998.
- [111] Sheng Xu and Z. Jane Wang. An immersed interface method for simulating the interaction of a fluid with moving boundaries. *Journal of Computational Physics*, 216(2):454–493, 2006.
- [112] L. Ying, G. Biros, and D. Zorin. A high-order 3d boundary integral equation solver for elliptic pdes in smooth domains. *Journal of Computational Physics*, 219:247–275, 2006.
- [113] David P. Young, Robin G. Melvin, Michael B. Bieterman, Forrester T. Johnson, Satish S. Samant, and John E. Bussioletti. A locally refined rectangular grid finite element method: application to computational fluid dynamics and computational physics. *Journal of Computational Physics*, 92(1):1–66, 1991.